

Space Weather

RESEARCH ARTICLE

10.1029/2020SW002583

This article is a companion to Sitnov et al. (2020), <https://doi.org/10.1029/2020SW002561>.

†Deceased 4 July 2020

Key Points:

- The biased data mining problem is mitigated by using weighted nearest neighbors, improving empirical reconstructions of the magnetic field
- Empirical distributions of storm time plasma pressure are obtained using a data mining reconstruction of the magnetic field
- The pressure retrieved from the empirical magnetic field is consistent with particle observations across species and energy channels

Correspondence to:

G. K. Stephens,
grant.stephens@jhuapl.edu

Citation:

Stephens, G. K., Bingham, S. T., Sitnov, M. I., Gkioulidou, M., Merkin, V. G., Korth, H., et al. (2020). Storm time plasma pressure inferred from multimission measurements and its validation using Van Allen Probes particle data. *Space Weather*, 18, e2020SW002583. <https://doi.org/10.1029/2020SW002583>

Received 6 JUL 2020

Accepted 12 OCT 2020

Accepted article online 19 OCT 2020

©2020. The Authors.

This is an open access article under the terms of the Creative Commons Attribution-NonCommercial-NoDerivs License, which permits use and distribution in any medium, provided the original work is properly cited, the use is non-commercial and no modifications or adaptations are made.

Storm Time Plasma Pressure Inferred From Multimission Measurements and Its Validation Using Van Allen Probes Particle Data

G. K. Stephens¹ , S. T. Bingham^{1†} , M. I. Sitnov¹ , M. Gkioulidou¹ , V. G. Merkin¹ , H. Korth¹ , N. A. Tsyganenko² , and A. Y. Ukhorskiy¹

¹Applied Physics Laboratory, The Johns Hopkins University, Laurel, MD, USA, ²Institute and Department of Physics, Saint Petersburg State University, Saint Petersburg, Russia

Abstract The k -nearest-neighbor technique is used to mine a multimission magnetometer database for a subset of data points from time intervals that are similar to the storm state of the magnetosphere for a particular moment in time. These subsets of data are then used to fit an empirical magnetic field model. Performing this for each snapshot in time reconstructs the dynamic evolution of the magnetic and electric current density distributions during storms. However, because weaker storms occur more frequently than stronger storms, the reconstructions are biased toward them. We demonstrate that distance weighting the nearest-neighbors mitigates this issue while allowing a sufficient amount of data to be included in the fitting procedure to limit overfitting. Using this technique, we reconstruct the distribution of the magnetic field and electric currents and their evolution for two storms, the intense 17–19 March 2015 “Saint Patrick’s Day” storm and a moderate storm occurring on 13–15 July 2013, from which the pressure distributions can be computed assuming isotropy and by integrating the steady-state force-balance equation. As the main phase of a storm progresses in time, the westward ring current density and pressure increases in the inner magnetosphere particularly on the nightside, becoming more symmetric as the recovery phase progresses. We validate the empirical pressure by comparing it to the observed pressures from the Van Allen Probes mission by summing over particle fluxes from all available energy channels and species.

1. Introduction

In situ measurements often provide only a small snapshot of a much larger and complex system. These observations must be interpreted and contextualized in order to gain physical insight. In contrast, statistical models seek to describe the global system by incorporating large sets of data, either by averaging or some other statistical processing. Empirical models have long sought to bridge these two approaches by describing the system using analytical expressions whose coefficients and parameters are then fit to data and in doing so establishing a framework in which to organize and contextualize data. The magnetosphere presents a unique challenge for empirical modeling as it is extremely large. Even limiting the domain to the near-Earth reconnection site, about $25 R_E$ down the tail, results in an object on the order of $\sim 10^4 R_E^3$ in volume. The magnetosphere is also dynamic, responding to changes in the solar wind environment in which it resides and organizing itself into several different global configurations. These events can last days in the case of geomagnetic storms but can also change as rapidly as tens of minutes during substorm expansions. Adding to the difficulty in empirical modeling is the extreme paucity of data within the magnetosphere, as there are at most only 10 to 20 spacecraft beyond low-Earth orbit with suitable scientific instrumentation.

Until recently, empirical magnetic field models were largely represented by the sets of custom-tailored modules with a predefined spatial structure (Tsyganenko, 2002a; Tsyganenko & Sitnov, 2005, and references therein). Each module reflected the theoretical view of the partial and symmetric ring current (PRC and SRC), tail, and field-aligned currents (FACs). A question is how to allow these models to respond to dynamical changes? Early models simply binned the magnetometer based on the K_p index and performed separate fits for each bin (Mead & Fairfield, 1975; Tsyganenko, 1989). These models did not smoothly transition between activity levels and instead simply jumped from one level to the next. Tsyganenko (1995, 1996) took a different approach, in which the amplitude coefficients of the individual modules were made functions of the solar wind parameters and the disturbance storm time (Dst) index. This had the advantage

that the model dynamics can evolve on the same cadence as the underlying input parameters. However, there are two primary shortcomings with this approach: First, the real magnetosphere does not respond instantaneously to the solar wind, and similarly, the solar wind inputs contain oscillations that are too fast for the real magnetosphere to react to. This was first addressed in Tsyganenko (2002b) where the solar wind inputs were averaged over the preceding hour. This technique was further advanced in Tsyganenko and Sitnov (2005), in which the simple hourly averages over preceding solar wind inputs were instead replaced with weighted averages by convolving the inputs with exponential functions. All these approaches still require ad hoc functional forms for the model amplitude coefficients and parameters as functions of the inputs regardless of how these inputs are combined, smoothed, and time averaged. The TS07D model (Sitnov et al., 2008) sought to eliminate these ad hoc driving functions by using a wholly different approach based on a simple albeit powerful data mining (DM) technique derived from the k -nearest-neighbors (KNN) method (Cover & Hart, 1967; Vassiliadis, 2006). Although the KNN method has traditionally been used for pattern classification, the TS07D model instead employed the algorithm as a way in which to mine magnetometer data and dynamically bin and fit the empirical model. In this method, the magnetic field model amplitude coefficients and nonlinear parameters are found by fitting them with only a small part (the K_{NN} nearest-neighbors or NNs) of the whole data base (with K_{DB} number of elements) that are most similar to the event of interest. By using $1 \ll K_{NN} \ll K_{DB}$, such an approach allowed the model to utilize many more measurements than are available at the moment of interest and enabled for a far more flexible magnetic field model. On the other hand, it also allowed the model to be made sufficiently sensitive to storm and substorm variability of the magnetosphere (Stephens et al., 2019; Tsyganenko & Sitnov, 2007) with the only ad hoc assumptions being the dipole tilt and solar wind dynamic pressure dependence (e.g., Tsyganenko & Sitnov, 2007).

The similarity of the NN events to the moment of interest is determined by their Euclidean distance in the state space formed by the global indices of activity, such as the *Sym-H* index and its time derivative, as well as the solar wind electric field (input) parameter vB_z , where $-v$ is the geocentric solar magnetospheric coordinate system (GSM) component of the solar wind bulk flow velocity and B_z is the z component of the interplanetary magnetic field (IMF). This new class of models allowed by the DM method (Sitnov et al., 2008; Tsyganenko & Sitnov, 2007) replaced tail and ring currents by regular expansions of the equatorial currents into systems of currents obtained from the general solution of Ampere's equation for an arbitrary thin equilibrium current distribution. Later a similar basis-element approach was applied to the FAC system (Sitnov et al., 2017).

The combination of the KNN DM algorithm with the Tsyganenko and Sitnov (2007) model allowed one to reconstruct different classes of storms driven by coronal mass ejections (CMEs) and corotating interaction regions (CIRs) (Sitnov et al., 2008, 2010). Moreover, Stephens et al. (2016) demonstrated that given more data and more elements in the model structure, TS07D resolves more features of the storm time magnetosphere, including the innermost eastward current and its closure on the night side forming the horseshoe or banana-like pattern (Liemohn et al., 2013; Roelof, 1989). The capabilities of this method were extended to the modeling of magnetospheric substorms (Sitnov, Stephens, et al., 2019; Stephens et al., 2019). It required the extension of the binning space (by adding the substorm index *AL* and its time derivative), adjustment of the averaging scales (to match substorm time scales), and the model structure (the use of complex equatorial current sheet structure with an embedded thin current sheet).

Moreover, the use of the steady-state force balance equation $\nabla P = \mathbf{j} \times \mathbf{B}$ allows one to reconstruct the plasma pressure P (Sergeev et al., 1994; Sitnov et al., 2018; Stephens et al., 2013; Tsyganenko, 2010). The empirical pressure derived from the reconstructed magnetic field can then be compared with the pressure reconstructed directly from plasma measurements (Mouikis et al., 2019; Sitnov et al., 2018), as the practically full coverage of the energy range for the ring current particles has become possible from the Van Allen Probes mission (Mauk et al., 2013). Comparison of the empirical pressure with the Van Allen Probes particle data showed impressive qualitative consistency (Sitnov et al., 2018). However, it also revealed a fundamental problem of the original DM approach: Since storms represent relatively rare events with the strongest variation of the DM metric parameters (e.g., *Sym-H*), their NN sets always have a bias toward more numerous weaker events in the NN bin (Sitnov et al., 2018, Figure 8). Another problem with the pressure validation is the necessity to map the observed in situ pressure from spacecraft's locations to the equatorial plane, where the pressure maps are usually computed.

In this paper we provide, for the first time, direct validation of the empirical pressure derived from the magnetic field data using TS07D algorithms and solve the aforementioned problems. First, we show that the NN bias toward weaker events can be well mitigated using the distance-weighted KNN method (e.g., Mitchell, 1997). In this method, the contribution of each NN in the data-fitting procedure is additionally weighted with larger weights for NNs closer to the query point. We also elaborated the algorithm of the pressure mapping from the selected probe to the equatorial plane along the field line using our magnetic field distribution. We compare the derived TS07D pressure with Van Allen Probes particle data for the July 2013 and March 2015 storms.

The structure of the paper is as follows. In section 2 we describe the architecture of the model including the NN data mining algorithm, introducing the novel distance-weighted NNs. Section 3 then discusses the empirical reconstruction of the plasma pressure applying it to the intense and frequently studied 17–19 March 2015 “Saint Patrick’s Day” storm. A technique is developed to map the Van Allen Probes ephemeris to the plasma reconstructions, allowing for a direct comparison between the empirical and observed pressures for this storm. We then apply the same analysis to a moderate and simpler event, the 13–15 July 2015 storm, and then look at the dependence of the reconstructed pressure on the direction of the integration path.

2. Data Mining Approach to Empirical Magnetic Field Modeling

The motivating principle driving the development of the TS07D flavor of empirical magnetic field models is that the data should dictate the model morphology rather than the model builder. This is fulfilled by first making the model (section 2.1) sufficiently flexible, for example, by describing equatorial currents using a regular expansion with no predefined azimuthal or radial structure. Second, the model evolves in time by fitting a small subset of the entire magnetometer database (section 2.2.3) identified by using a simple albeit powerful data mining technique (KNN) as described in section 2.2. This paper along with the companion study on extreme events (Sitnov et al., 2020) employ a technique to account for the inhomogeneity of the NNs, termed distance-weighted NNs (section 2.2.5).

2.1. Model Architecture

A key element of the TS07D modeling approach was to replace the ad hoc description of the magnetic field from the SRC, PRC, and tail current with a single expansion derived from the general solution of the magnetic vector potential for a flat thin current sheet (Tsyganenko & Sitnov, 2007). The resulting magnetic field has the form

$$\mathbf{B}_{\text{sheet}}(\rho, \phi, z) = \sum_{n=1}^N a_{0n}^{(s)} \mathbf{B}_{0n}^{(s)} + \sum_{m=1}^M \sum_{n=1}^N \left(a_{mn}^{(o)} \mathbf{B}_{mn}^{(o)} + a_{mn}^{(e)} \mathbf{B}_{mn}^{(e)} \right) \quad (1)$$

where $\mathbf{B}_{0n}^{(s)}$, $\mathbf{B}_{mn}^{(o)}$, and $\mathbf{B}_{mn}^{(e)}$ are the basis functions, where these fields are the curl of the magnetic vector potential solution. The scalars $a_{0n}^{(s)}$, $a_{mn}^{(o)}$, and $a_{mn}^{(e)}$ are amplitude coefficients which are determined when the model is fit to data. M represents the number of azimuthal (sine and cosine terms) expansions, while N represents the number of radial (Bessel functions) expansions. The chosen value of M and N differs on model application and the amount of data used in the fit. Increasing these values results in higher model resolution but too high a value results in overfitting. The initial storm time investigations (Sitnov et al., 2008, 2010) used $(M, N) = (4, 5)$, while later studies (Stephens et al., 2016) enhanced the model resolution by increasing the number of terms to $(M, N) = (6, 20)$ and by incorporating additional spacecraft magnetometer data sets. The equatorial current sheet thickness comes about by replacing $|z|$ with $\zeta = \sqrt{z^2 + D^2}$ in the vector potential solution for a thin current sheet, where D represents a characteristic half thickness and is a free parameter determined during the fit. However, during active times the current sheet thickness does not have a single characteristic scale tail (Sitnov, Birn, et al., 2019, and references therein). This is rectified by combining two separate expansions, one initialized to a relatively thick ($D \approx 2.0 R_E$) and the other one to a relatively thin ($D_{TCS} \approx 0.5 R_E$) half thickness (Stephens et al., 2019). The idealized equatorial magnetic field is now the sum of the thick and thin sheets.

$$\mathbf{B}_{eq,0}^{(u)}(\mathbf{r}_0^{(u)}) = \mathbf{B}_{sheet}(\rho, \phi, z; D) + \mathbf{B}_{sheet}(\rho, \phi, z; D_{TCS}) \quad (2)$$

where D and D_{TCS} are treated as free parameters in the fit. The (u) notation used here is to indicate that this field does not yet account for the dipole tilt effects; that is, it represents a perfectly flat untilted (or unwarped) sheet, and the naught symbol indicates that the field does not yet account for the dynamic pressure effects. The additional thin current sheet has been critical in reconstructing the eastward ring current particularly during the early main and late recovery storm phases when the magnitude of the current density is low. The eastward current is of particular importance in this study as the boundary between the eastward and westward currents determine the location of the pressure peak. However, this doubles the number of coefficients used to determine the equatorial structure. Because of this, the number of azimuthal expansions is reduced by a factor of 2 from $M = 6$ to $M = 3$ resulting in a resolution of $(M, N) = (3, 20)$. In contrast, in the companion paper on extreme events (Sitnov et al., 2020), where there are relatively few events from which to draw data, the additional current sheet proved unnecessary as the current densities were very large and was not included. Thus, that study has retained the Stephens et al. (2016) resolution of $(M, N) = (6, 20)$.

Similarly, the FAC is also constructed using a Fourier expansion in local time based on the conical current model described by Tsyganenko (1991). This formulation of the FAC system is then copied to various latitudes to achieve flexibility in both latitude and local time (Sitnov et al., 2017). Here, the configuration from Stephens et al. (2019) is used, which incorporates the first four Fourier harmonics for each of four systems centered at different latitudes for a total of 16 amplitude coefficients (4 harmonics/system \times 4 systems) that determine the azimuthal and latitudinal structure of the FACs, which is sufficient (e.g., see Figures 4–6 in Stephens et al., 2019) for reconstructing the realistic FAC morphology as determined by low altitude spacecraft magnetometers (Murphy et al., 2013). From here, the general deformation technique (Stern, 1987; Tsyganenko, 1998) is applied using the transformations detailed by Tsyganenko (2002a, 2002b). This bends the radially directed conical current sheets into a shape that approximates the realistic terrestrial field line morphology including the day-night asymmetry. The final step is to scale the systems by a global scaling $\mathbf{B}_{FAC,0}(\mathbf{r}_0) = \kappa \mathbf{B}'_{FAC}(\kappa \mathbf{r})$. The two higher latitude and the two lower latitude systems are scaled independently, introducing two free parameters into the fit κ_{R1} and κ_{R2} . This allows the systems expand and contract with magnetospheric activity level and solar wind conditions as is observed by the AMPERE mission (Anderson et al., 2008, 2014; Clausen et al., 2012).

Each of these current systems along with the intrinsic field is then complemented with shielding fields which act to contain the total magnetic field within the magnetopause boundary, that is to ensure $\mathbf{B}_{tot} \cdot \mathbf{n}|_S = 0$ (Tsyganenko, 2013, and references therein), where S is the modeled magnetopause surface and n is the normal to that surface.

The only remaining major ad hoc assumptions in the model architecture are in how the current systems deform due to changes in the dipole tilt angle and how the magnetopause boundary and current systems expand and contract in response to changes in the solar wind dynamic pressure. A way to handle the dipole tilt angle effects is by applying the aforementioned general deformation technique (Stern, 1987; Tsyganenko, 1998). For example, here the “bowl-shaped” deformation (Tsyganenko, 2014) describes for the dipole tilt effects on the equatorial field \mathbf{B}_{eq} and its shielding field $\mathbf{B}_{eq}^{(sh)}$, introducing three more nonlinear parameters into the fitting routine, the hinge distance R_H , the warping parameter G , and the twisting parameter TW . This works by defining a point transformation that takes position vectors from the dipole tilt deformed space \mathbf{r}_0 to the untilted space (represented in Equation 2) $\mathbf{r}_0^{(u)}$, that is an analytical function $\mathbf{r}_0^{(u)}(\mathbf{r}_0)$ is defined. The general deformation technique then yields the resulting dipole tilt deformed equatorial magnetic field $\mathbf{B}_{eq,0}(\mathbf{r}_0) = \hat{\mathbf{T}} \cdot \mathbf{B}_{eq,0}^{(u)}(\mathbf{r}_0^{(u)}(\mathbf{r}_0))$, where $\hat{\mathbf{T}}$ is a tensor composed of the partial derivatives of $\mathbf{r}_0^{(u)}(\mathbf{r}_0)$.

It is often desired to visualize the model outputs and to compute magnetic field derived quantities (such as the pressure) along the magnetic equator. This can readily be achieved by setting $\Psi = TW = 0$ which effectively nullifies all the dipole tilt angle effects, thus aligning the magnetic equator and the center of the current sheet with the equatorial plane and making the model north-south symmetric, termed here as the untilted model $\mathbf{B}_{tot}^{(u)}$. Magnetic equator visualizations shown in subsequent figures are simply equatorial slices performed using the untilted model. Empirical studies of the magnetopause boundary have shown

that, at least to first order, it expands and contracts in a self-similar way in response to changes in the solar wind dynamic pressure P_{Dyn} (Shue et al., 1998); that is, changes in size are described by a rescaling of the position vector $\mathbf{r}_0 = \mathbf{r}_{GSM} \left(\frac{P_{Dyn}}{P_{Dyn,0}} \right)^\kappa$, where $P_{Dyn,0}$ is the baseline dynamic pressure, often taken to be $P_{Dyn,0} = 2$ nPa and here κ is taken to be 0.155 which is similar to the value found in the empirical studies performed by Shue et al. (1998). Thus, the external magnetic field in the GSM coordinate system is found by rescaling the external fields described above $\mathbf{B}_{ext}(\mathbf{r}_{GSM}) = \mathbf{B}_{ext,0}(\mathbf{r}_0)$. Likewise, the equivalently scaled untilted model is given as $\mathbf{B}_{ext}^{(u)}(\mathbf{r}^{(u)}) = \mathbf{B}_{ext,0}^{(u)}(\mathbf{r}_0^{(u)})$. Furthermore, the dynamic pressure is explicitly incorporated into the equatorial field by replacing the amplitude coefficients in Equation 1 by $a_{\alpha\beta}^{(\gamma)} \rightarrow a_{0,\alpha\beta}^{(\gamma)} + a_{1,\alpha\beta}^{(\gamma)} \sqrt{P_{Dyn}}$, thus doubling their number.

Thus, the modeled total magnetic field is $\mathbf{B}_{tot} = \mathbf{B}_{int} + \mathbf{B}_{int}^{(sh)} + \mathbf{B}_{eq} + \mathbf{B}_{eq}^{(sh)} + \mathbf{B}_{FAC} + \mathbf{B}_{FAC}^{(sh)}$. The commonly used IGRF model (Thébault et al., 2015) is used for the internal field \mathbf{B}_{int} and is not included in the fit.

2.2. Data Mining

2.2.1. NN Binning

It is assumed that the state of the magnetosphere can be characterized by some multidimensional time-dependent state vector $\mathbf{G}(t)$ (Vassiliadis, 2006), the components of which are macroscopic properties of the magnetosphere, such as geomagnetic indices, solar wind conditions, and/or their time derivatives. Analogous to classical mechanics, the time derivatives are critical to capturing the dynamics of the system. For example, the *Sym-H* index indicates the level of geomagnetic storm activity, but its time derivative is necessary to differentiate between the main and recovery phases of a storm. As the magnetosphere evolves in time, this state vector traces curves within the state space; see the sketch in Figure 1a (blue curves). In particular, magnetospheric disturbance modes, such as storms and substorms, are expected to follow curves in a state space customized to describe them (section 2.2.2). Once discretized in time to a particular cadence (in this case all parameters are discretized to a 5 min cadence) these curves become a cloud of individual points (Figure 1a; hollow red circles).

Now, for some moment of interest $t = t'$ there are on the order of ~ 10 or less spacecraft magnetometers providing measurements. This is far too few to fit a flexible empirical magnetic field model like the one described above. However, in the state space, there are potentially many more points in relatively close proximity to the point of interest $\mathbf{G}(t')$. The K_{NN} points that are closest to the point of interest $\mathbf{G}(t')$ form a set of NNs $\{\mathbf{G}(t_i)\}$, as shown in Figure 1b by the filled red circles. For simplicity, the standard Euclidean distance metric (shown by the red arrow)

$$R(t_i) = \left(\sum_{j=1}^{M_B} \delta_j \left(\frac{\mathbf{G}_j(t_i) - \mathbf{G}_j(t')}{\sigma_{G_j}} \right)^2 \right)^{\frac{1}{2}} \quad (3)$$

is used to measure the distance from the point of interest $\mathbf{G}(t')$ to the NN with the following modifications. First, the components \mathbf{G}_j of the state vector $\mathbf{G}(t)$ may have very different scale lengths; thus, each component should be normalized to make the scale lengths roughly similar. Here, the components are normalized by their standard deviations computed over the entire state space. Second, some components may be more critical in capturing particular dynamics, so a weighting δ_j is introduced that will bias the distance metric toward or away from particular components. For simplicity, here, as with all previous works, components are weighted equally to unity $\delta_j = 1$. The size of the NN multidimensional sphere R_{NN} (blue line) is defined to be the NN furthest away from the point of interest (blue arrow in Figure 1b).

In order to properly constrain the model, K_{NN} must be larger than the number of degrees of freedom the model has. However, in order for the set of NNs to resemble the dynamical process being investigated, K_{NN} must be much less than the total number of points in the state-space K_{SS} . The magnetometer database used in this study (presented below in section 2.2.3) spans 21 years, which at 5 min cadence equates to $K_{SS} \approx 2 \times 10^6$.

The points in the set of NNs $\{\mathbf{G}(t_i)\}$ form segments of curves in the state space, each of which corresponds to a time interval (dashed lines in Figure 1d). These time intervals are intersected with the magnetometer

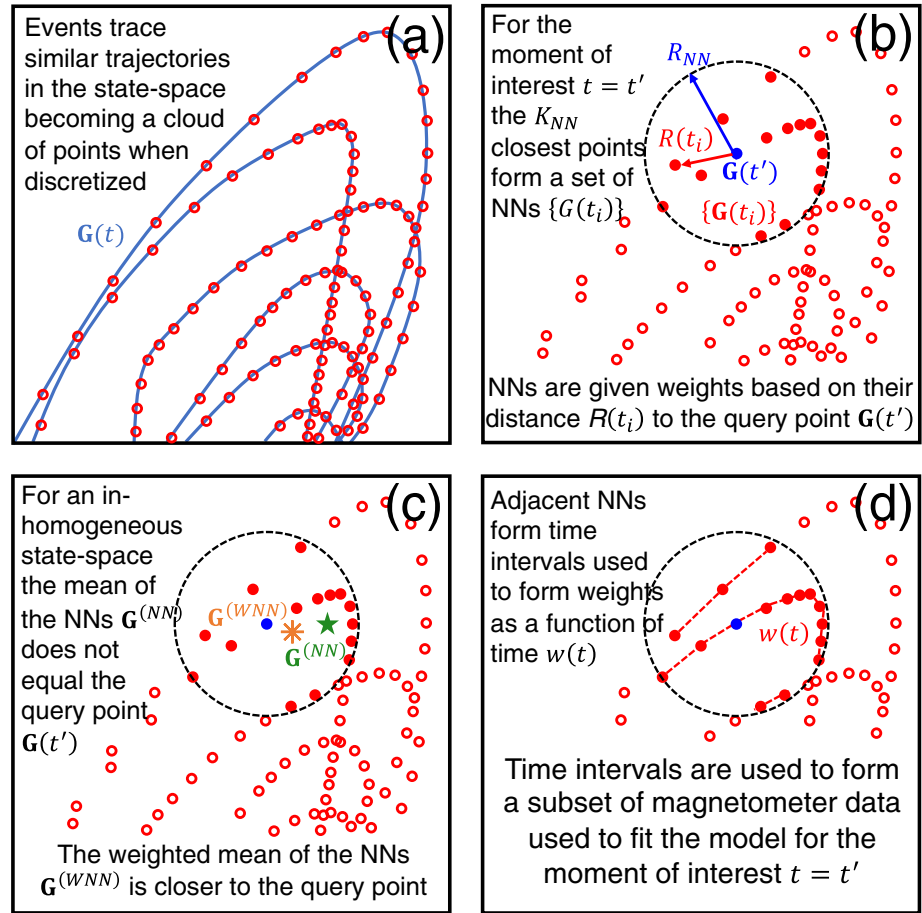


Figure 1. (a–d) A schematic demonstrating the distance-weighted NN binning algorithm. Here trajectories are shown in a 2-D state space based on the trajectories geomagnetic storms trace in a state-space composed of the *Sym-H* index and its derivative. In an inhomogeneous state space the mean of the NNs tends to not match the query point. Giving closer NNs larger weights results in a weighted mean that is closer to the query point. These weights are then used during the fitting procedure by attaching them to the corresponding magnetometer data.

database to form a subset of data that are from times when the magnetosphere was presumably in a similar configuration as the moment of interest. This subset of data is then used to fit the model (section 2.2.4) for that particular moment. For the reconstruction of an entire event, each moment in time (5 min cadence is again used) gets its own subset of data and corresponding fit, thus, giving the model its dynamical nature.

2.2.2. The Magnetospheric Storm State Space

A benefit of the KNN technique is that the state space can be customized to the events of interest. A variety of dynamical events can be studied simply by formulating a new state space that captures the signatures of these events. The state space for storms $\mathbf{G}^{(s)}$ is formulated below.

A defining characteristic of geomagnetic storms is the buildup and enhancement of the ring current, typically occurring over several hours to a couple of days for multistage events, and its gradual decay over the proceeding days (Gonzalez et al., 1994, and references therein). The TS07D state space (Sitnov et al., 2008) was tailored to storms and was based on the Burton-McPherron-Russell formalism (Burton et al., 1975) which relates the solar wind electric field parameter vB_z^{IMF} and the storm magnetic index *Dst* and its derivative. This storm time state space is $\mathbf{G}^{(s)}$ given by

$$G_1^{(s)}(t) = \langle \text{Sym-H}^* | \propto \int_{-\Pi_s/2}^0 \text{Sym-H}^*(t + \tau) \cos(\pi\tau/\Pi_s) d\tau \quad (4)$$

$$G_2^{(s)}(t) = D\langle \text{Sym-H}^* | / Dt \propto \int_{-\Pi_s/2}^0 \text{Sym-H}^*(t + \tau) \cos(2\pi\tau/\Pi_s) d\tau \quad (5)$$

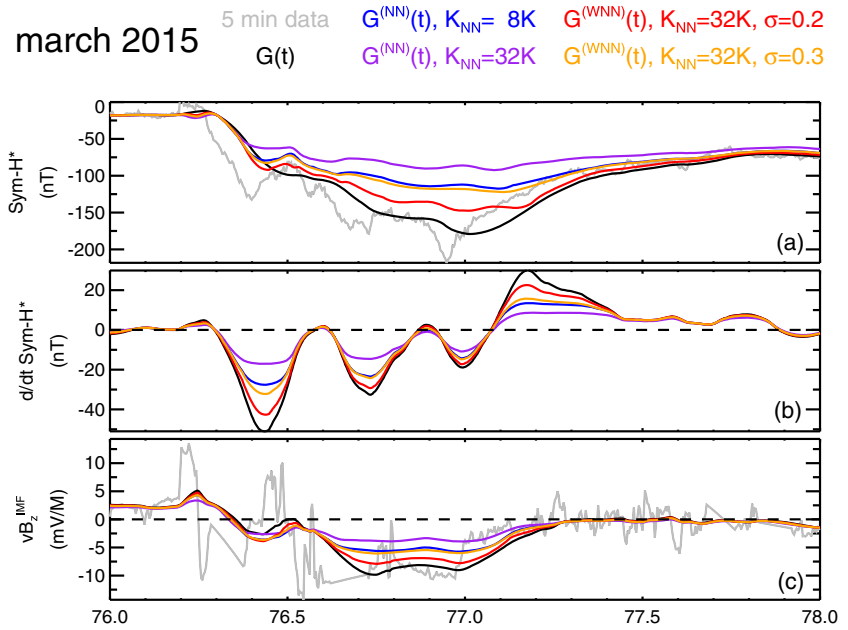


Figure 2. Time series plots of the storm state-space for the 17–19 March 2015 geomagnetic storm, the strongest storm during the Van Allen Probes mission. The original 5 min cadence data are shown in gray, and the corresponding unnormalized state-space parameters are overplotted in black. The means of the state-space parameters over the set of nearest neighbors are shown in blue and purple corresponding to $K_{NN} = 8,000$ and $K_{NN} = 32,000$, respectively. The weighted means of the state-space parameters over the set of nearest neighbors with $K_{NN} = 32,000$ are plotted in red and orange using a Gaussian weighting function with $\sigma = 0.2$ and $\sigma = 0.3$, respectively. The storm state space is composed of three parameters, (a) the pressure corrected storm index ($Sym-H^*$), (b) the time derivative of $Sym-H^*$, and (c) the solar wind electric field parameter vB_z^{IMF} .

$$G_3^{(s)}(t) = \langle vB_z^{IMF} | \propto \int_{-\Pi_s/2}^0 vB_z^{IMF}(t + \tau) \cos(\pi\tau/\Pi_s) d\tau \quad (6)$$

where $Sym-H$ is an index of the storm activity. It is determined from averaging midlatitude ground based magnetometers (Iyemori, 1990) from across the globe and is higher cadence analog of the widely used Dst index. A shortcoming of this index is that it simultaneously captures magnetic perturbations from the ring current but also magnetopause and induction currents. The ring current contributions can be approximately isolated by applying the following correction $Sym-H^* = A \cdot Sym-H - B \cdot (P_{dyn})^{1/2}$ (Gonzalez et al., 1994, and references therein) where the values A and B are taken to be 0.8 and 13.0, respectively (Tsyganenko, 1996). The solar wind electric field parameter vB_z^{IMF} is the X_{GSM} component of the solar wind bulk flow velocity multiplied by the Z_{GSM} component of the solar wind IMF time propagated to the bow shock nose. This parameter has long been known to be correlated with both storm and substorm activity (Newell et al., 2007, and references therein). The integration in Equations 4–6 convolves the time series data with half cosine function of width $\Pi_s = 12$ hr, which smooths the original data to storm time scales. The notation $\langle \dots |$ (Sitnov et al., 2012) indicates that the smoothing windows are only applied over past data (note the limits on the integrals). This was done because a symmetric smoothing window $\langle \dots \rangle$ results in a smoothed time series which reacts to changes that have not yet occurred. The $D\langle \dots \rangle / Dt$ notation represents a smoothed time derivative, which is achieved by halving the period of the convolution window while keeping the integration limits the same. For a more detailed discussion on the topic of smoothing windows, see Sitnov et al. (2012) in particular their Figure 2 for a schematic.

The components of the storm state space vector $G^{(s)}$ are plotted for the March 2015 geomagnetic storm in Figure 2 (black lines). This storm was chosen as it is the strongest to occur during the Van Allen Probes mission, reaching a $Sym-H$ minimum of -233 nT, and because it was previously reconstructed using an earlier iteration of the class of model presented here (Sitnov et al., 2018). The smoothing windows effectively remove the substorm scale oscillations in $Sym-H$ and vB_z^{IMF} . The main phase of the storm contains three distinct stages, as indicated by the $D\langle Sym-H^* \rangle / Dt$ parameter.

Throughout this discussion and throughout the study as a whole, the bow shock nose propagated solar wind parameters P_{dyn} and vB_z^{IMF} are obtained from the 5 min cadence OMNI database (https://omniweb.gsfc.nasa.gov/ow_min.html) which are derived from the IMP-8, ACE, WIND, Geotail, and DSCOVR missions. The $Sym-H$ and AL indices are also contained within the 5 min OMNI database but are compiled from the World Data Center for Geomagnetism, Kyoto (<http://wdc.kugi.kyoto-u.ac.jp/>).

2.2.3. Spacecraft Magnetometer Database

This study utilizes the spacecraft magnetometer database from Sitnov, Stephens, et al. (2019) which is nearly identical to the database constructed for the substorm analysis in Stephens et al. (2019) with the only difference being that the former added the 2016–2017 magnetometer data from the MMS mission (four probes). The construction of this data set was meant to overlap with the advent of continuous solar wind monitoring following the launch of the WIND spacecraft in late 1994. The database includes the THEMIS (five probes) and Van Allen (two probes) missions which sample the equatorial inner magnetosphere region, including the vicinity of the eastward current system ($2 R_E \leq r \leq 4 R_E$) which is crucial to resolving the peak in the plasma pressure, along with the geosynchronous orbiting ($r \sim 6.6 R_E$) GOES (08, 09, 10, and 12) spacecraft. The midtail region $12 R_E \leq r \leq 22 R_E$ has a noticeable drop in data coverage, as only two of the THEMIS probes were ever located here and only for about 2 years before then were moved into a lunar orbit becoming the ARTEMIS mission. With an apogee of $r \sim 18 R_E$, the Cluster mission (four probes) helps populate this region; however, as a polar-orbiting spacecraft, they spent a limited amount of time in the equatorial region. Beyond $22 R_E$ the data density drops off by nearly an order of magnitude as the only spacecraft in the database that spent a considerable time in this region were the Geotail and MMS missions. The only other spacecraft included in the database is IMP-8; however, it comprises a relatively small amount of the total data set.

2.2.4. Fitting the Model

Once the subset of spacecraft magnetometer data has been identified, the various nonlinear parameters (D , D_{TCS} , κ_{R1} , κ_{R2} , R_H , G , and TW) and linear amplitude coefficients are fit. The nonlinear parameters are fit using the Nelder-Mead downhill simplex method (Press et al., 1992) by minimizing the objective function:

$$M_{err}^{(NN)} = \sqrt{\sum_{j \in S_{NN}} \sum_{i=x,y,z} w_j w_{(0)}(r) [B_i^{(mod)}(\mathbf{r}_{GSM}^{(j)}) - B_i^{j,obs}]^2} \quad (7)$$

where S_{NN} is the identified subset of the magnetometer data and $B_i^{j,obs}$ are the corresponding components of the observed external magnetic field. $B_i^{(mod)}(\mathbf{r}_{GSM}^{(j)})$ are the components of the modeled external magnetic field computed at the spacecraft's location $\mathbf{r}_{GSM}^{(j)}$. The measurements are weighted by the product $w_j w_{(0)}(r)$, where $w_{(0)}(r)$ is a radial weighting meant to correct for the inhomogeneous distribution of data in space, that is regions with a high data density such as near geosynchronous orbit receive small weights while the midtail region receives a higher weight. See Tsyganenko and Sitnov (2007) section 5.2 for a more complete discussion on this topic. The additional weighting w_j is being introduced here and in the companion extreme event study for the first time. Weights are assigned values based on the distance $R(t_i)$ between the point of interest $\mathbf{G}(t')$ and the corresponding position of that magnetometer measurement in the state space $\mathbf{G}(t_i)$ as will be described in the next section. The linear amplitude coefficients are determined by solving the linear least squares problem for an overdetermined system (Press et al., 1992) using a singular value decomposition (SVD) to eliminate overly small singular values, with the same weights used in Equation 7.

2.2.5. Distance-Weighted NNs

In a homogenous state space the mean of the set of NNs $\mathbf{G}^{(NN)}$ should approximately coincide with the point of interest:

$$\mathbf{G}(t') \approx \mathbf{G}^{(NN)} \equiv \frac{1}{K_{NN}} \sum_{i=1}^{K_{NN}} \mathbf{G}(t_i). \quad (8)$$

However, magnetospheric macroscopic variables, such as solar wind parameter values or geomagnetic indices, are highly inhomogeneous during active conditions. The result is that the magnitude of $\mathbf{G}^{(NN)}$ tends to be smaller than the magnitude of $\mathbf{G}(t')$ during active times as is sketched in Figure 1c (green star). This can

be mitigated by decreasing the number of NNs K_{NN} (note how the blue line more closely tracks the black line as compared to the purple line in Figure 2); however, too few NNs lead to overfitting or require an overly simplified model. For example, in order to effectively describe substorms (Stephens et al., 2019), the number of NNs was increased from $K_{NN} = 8,000$ to $K_{NN} = 32,000$. This results in a dilemma, in order to have enough data to reconstruct the spatial structure associated with storms and/or substorms without overfitting, a large K_{NN} is required, but a large K_{NN} pulls the model away from the event of interest and biases the model toward less extreme events. This effect is illustrated in Figure 2. Note how the mean over the set of NNs of the components of $\mathbf{G}^{(NN)}$ (blue and purple lines) consistently underestimates the magnitude of the components of \mathbf{G} (black lines), with the gap becoming larger as the magnitude of \mathbf{G} increases. For example, in Figure 2a the minimum $\langle \text{Sym-}H^* \rangle$ value is -179 nT while it only reaches -118 nT for $\mathbf{G}^{(NN)}$ with $K_{NN} = 8,000$ and only -92 nT with $K_{NN} = 32,000$.

An effective mitigation to this issue was found by distance weighting the NNs using a simple Gaussian function of the distance $R(t_i)$ between the NN $\mathbf{G}(t_i)$ and the point of interest $\mathbf{G}(t')$.

$$w_i = e^{-\frac{x_i^2}{2\sigma^2}}, \quad x_i = \frac{R(t_i)}{R_{NN}} \quad (9)$$

Thus, the weighted average of the set of NNs is given by

$$\mathbf{G}^{(WNN)} \equiv \frac{\sum_{i=1}^{K_{NN}} w_i \mathbf{G}(t_i)}{\sum_{i=1}^{K_{NN}} w_i}. \quad (10)$$

The impact of this distance-weighting technique (sketched in Figure 1c as the orange asterisk) is demonstrated in Figure 2. The weighted components of $\mathbf{G}^{(WNN)}$ with $K_{NN} = 32,000$ and $\sigma = 0.3$ (orange line) now performs similarly to $\mathbf{G}^{(NN)}$ with $K_{NN} = 8,000$ (blue line). Smaller values of σ result in a narrower Gaussian and yield even better consistency with \mathbf{G} , for example, the components of $\mathbf{G}^{(WNN)}$ using $\sigma = 0.2$ (red line) now perform better than $\sigma = 0.3$ (orange line). The minimum $\langle \text{Sym-}H^* \rangle$ value for the weighted averages are now -122 and -147 nT for $\sigma = 0.3$ and $\sigma = 0.2$, respectively.

As described before and represented in Figure 1d, adjacent NNs form intervals in time, which are then intersected with the magnetometer database to form a subset of the data that is used to fit the model for that moment of interest. Since each NN is now assigned a weight w_i , the weights as a function of time $w(t)$ can be constructed by a simple linear interpolation. Each magnetometer record in the subset of data can similarly be assigned a weight to be used in the objective function, represented as w_j in Equation 7.

In order to demonstrate the impact distance-weighted NNs has on the model, it was fit to each of the four configurations shown in Figure 2 for the moment 18 March 2015, 00:00 (day of year 77.0), which is close to the $\langle \text{Sym-}H^* \rangle$ minimum for the storm. Thus, this time represents a particularly extreme scenario, in which the weighting algorithm described above is most useful. The current density is plotted for these configurations in Figure 3. In this figure and throughout the work current densities are numerically evaluated from the modeled magnetic field via Ampere's law $\mu_0 \mathbf{j} = \nabla \times \mathbf{B}$. To emphasize the problem of overfitting, a higher resolution $(M, N) = (6, 20)$ was used in constructing this figure instead of $(M, N) = (3, 20)$ which is used throughout the rest of this study. Comparing panel (a) to panel (b) reveals that the $K_{NN} = 8,000$ configuration includes artifacts due to overfitting throughout the tail. Increasing K_{NN} to 32,000 reduces these artifacts and yields a smoother overall picture, but at the expense of a significantly decreased ring current near geosynchronous orbit. The weighted $K_{NN} = 32,000$ with $\sigma = 0.3$ (panel d) configuration effectively eliminates many of these artifacts, while maintaining the strong ring current from the unweighted $K_{NN} = 8,000$ configuration (panel a). However, panel (c) demonstrates the limitations to this approach. The $K_{NN} = 32,000$ with $\sigma = 0.2$ configuration introduces numerous artifacts, presumably as many of the NNs (and by extension magnetometer data) effectively have a zero weight. Based on these results, $\sigma = 0.3$ will be used for the remainder of this study and also will be the value used in the companion extreme events study (Sitnov et al., 2020). Different distributions with broader tails, such as the Student's t distribution, may yield even better results, but this will be left for future studies.

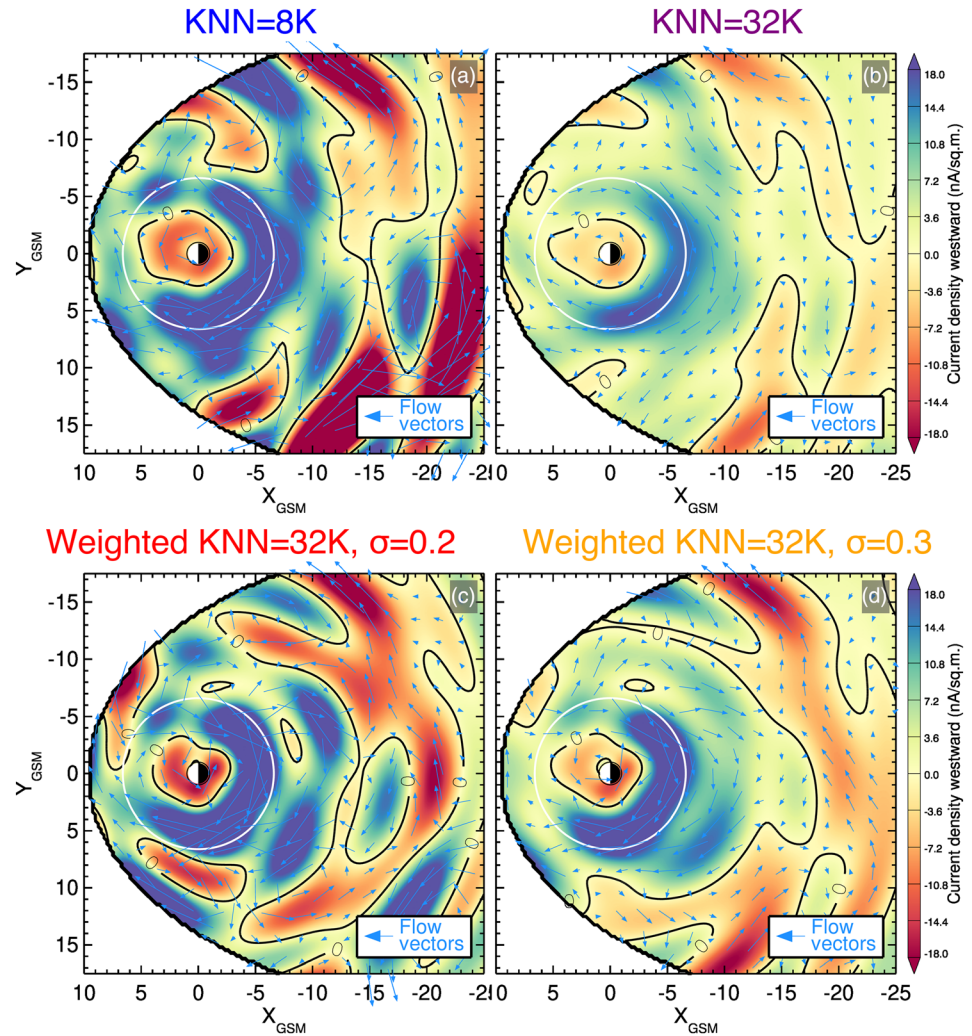


Figure 3. Equatorial current density plots demonstrating the impact K_{NN} and the distance-weighted NN algorithm has on the model for a particularly extreme moment (18 March 2015, 00:00) during the March 2015 geomagnetic storm. The configurations are (a) unweighted NNs $K_{NN} = 8,000$, (b) unweighted NNs with $K_{NN} = 32,000$, (c) Gaussian weighted $K_{NN} = 32,000$ and $\sigma = 0.2$, and (d) Gaussian weighted $K_{NN} = 32,000$ and $\sigma = 0.3$. To emphasize the problem of overfitting, a higher resolution $(M, N) = (6, 20)$ was used. The color represents westward component of the current density field, with green-blue representing westward and orange-red eastward flowing electric currents. The zero contour is overplotted in black. Flow vectors are overplotted in blue, indicating the direction and magnitude of the current flow. In order to simplify the visualizations, the untilted version of the model is used, where dipole tilt and twist effects are ignored, thus aligning the magnetic equator with the equatorial plane. All subsequent equatorial slices will do the same.

3. Pressure Reconstruction During Geomagnetic Storms

The empirical reconstruction of the plasma pressure in the inner magnetosphere is obtained using the afore-described data mining-driven empirical magnetic field model for two geomagnetic storms. First, the intense 17–19 March 2015 “Saint Patrick’s Day” storm is reconstructed. Given the complex nature of that event, a moderate and simpler storm occurring on 13–15 July 2013 is then analyzed.

3.1. Line Integral Computation of the Plasma Pressure

The inner magnetosphere is often assumed to be in a quasi-static equilibrium (Vasyliunas, 1970; Wolf, 1983):

$$\nabla P = \mathbf{j} \times \mathbf{B}. \quad (11)$$

If the magnetic field is dotted with this: $\mathbf{B} \cdot \nabla P = \mathbf{B} \cdot (\mathbf{j} \times \mathbf{B}) = 0$ since the magnetic field is orthogonal to $\mathbf{j} \times \mathbf{B}$. Thus, a consequence of the isotropic pressure assumption is that the pressure is constant along

magnetic field lines. This reduces the pressure computation to a 2-D problem; that is, if the pressure is known on a 2-D plane along with the 3-D magnetic field, the pressure can be mapped to 3-D by tracing along magnetic field lines.

The force balance equation can be solved using the fundamental theorem of calculus for line integrals:

$$\int_C \nabla P(\mathbf{r}') \cdot d\mathbf{r}' = P(\mathbf{r}) - P(\mathbf{r}_0) = \int_C (\mathbf{j} \times \mathbf{B}) \cdot d\mathbf{r}' \quad (12)$$

where the path C is a smooth curve along which ∇P is continuous. The integration is begun at some point \mathbf{r}_0 where the pressure is presumably known or is small enough that it can be neglected, and the point where the pressure is desired is given as $P(\mathbf{r})$. In order to simplify these computations, the untilted model $\mathbf{B}_{\text{tot}}^{(u)}$ (section 2.1) is used, allowing the integration to be performed entirely in the equatorial plane. Thus, the solution obtained is the untilted pressure field $P^{(u)}(\mathbf{r}^{(u)})$. A technique for generalizing the untilted pressure field to a field in geophysical coordinates, in this case GSM, will be presented below in section 3.2.1.

3.2. March 2015 Storm Reconstruction

The previously mentioned (Figures 2 and 3) 17–19 March 2015 “Saint Patrick’s Day” event was the strongest storm to occur during the Van Allen Probes era. In March of that year the Van Allen Probes were in a tail orbital configuration, making this an ideal test case to observe particle loss, acceleration, and transport processes in the inner-magnetosphere during a CME-driven storm (e.g., Baker et al., 2016). This storm included three distinct main phases (Figure 2b), and particle observations indicate that energetic ions and oxygen played an important role in the buildup and intensity of the ring current and pressure particularly during the third step of the main phase (Keika et al., 2018). Additionally, the TWINS mission measured energetic neutral atoms (ENAs) reconstructing a pressure peak form at $r \approx 3 - 4 R_E$ (Perez et al., 2016) during the main phase.

The Van Allen Probes’ orbit was in a tail configuration during this event with an apogee centered about ~ 22 MLT. The comparison between the modeled field and magnetic field measurements from the Van Allen Probes EMFISIS instrument (Kletzing et al., 2013) are displayed in Figures 4a–4h. The large negative dips in external B_z are located in the region that transitions between the westward and eastward current systems ($r \approx 4 R_E$). Many of these dips are reconstructed, although the magnitude of several of them is significantly underestimated by the model. One explanation is that, although the distance-weighting mitigates the issue, the weighted average of the NNs $\mathbf{G}^{(WNN)}$ still underestimates the actual intensity of $\langle \text{Sym-}H^* \rangle$ throughout much of the storm (the gap between the black and orange lines in Figure 2a). Another is that the magnitude of these dips is caused by localized currents whose radial size is too small to be reconstructed using this method. Other large deviations occur in the value of B_y . One possible source of this discrepancy is that during the main phase and early recovery phase of this storm the solar wind contained a large magnitude of B_y^{MF} . The Cluster and THEMIS missions also made magnetometer observations (Auster et al., 2008; Balogh et al., 1997) during this event, although they were in dayside configurations at the time, so they were located outside the magnetopause for much of the duration of the storm, indicated by the large gaps for those spacecraft in Figure 4. The other Cluster and THEMIS probes are omitted from the figure because they were in a similar orbital configuration as the probes indicated and thus had similar validation plots and were redundant. Overall, both missions displayed good agreement between the model and the data as displayed Figures 4i–4p.

3.2.1. March 2015 In Situ Pressure Validation

The Van Allen Probes mission provides a unique opportunity to validate the empirical pressure computation. The twin probes were located in a near equatorial orbit with a perigee altitude of ~ 600 km and an apogee of $\sim 5.8 R_E$, meaning they flew directly through the pressure peak. The orbital period was ~ 9 hr resulting in several orbits during the course of a geomagnetic storm. While each spacecraft had a nearly identical orbit, Van Allen Probe A had a slightly shorter orbital period, so that it lapped Probe B every 75 days. Most importantly, the particle suite spanned a wide range of energies and species, allowing for a good estimate of the total in situ plasma pressure (Mauk et al., 2013).

The Van Allen Probes’ pressures for this event have been calculated using observations from the helium, oxygen, proton, and electron (HOPE) instrument (Funsten et al., 2013) from the ECT suite (Spence et al., 2013)

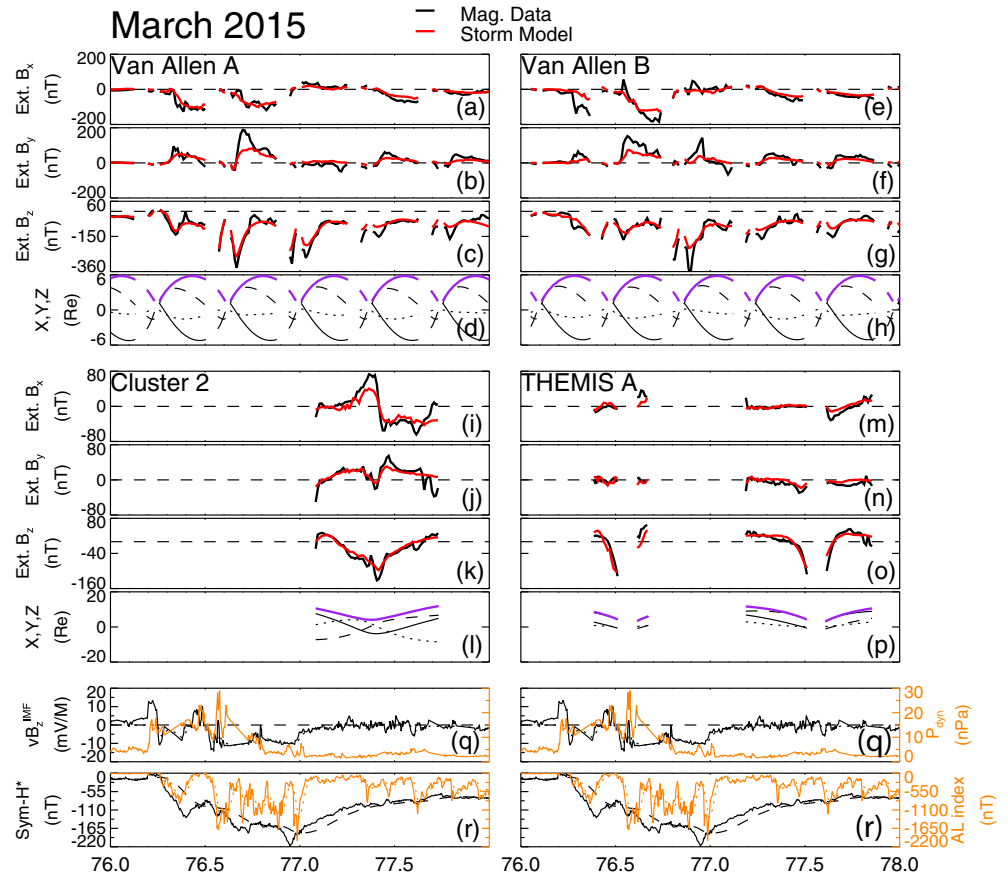


Figure 4. Comparison between the observed magnetic field from the Van Allen Probes, Cluster, and THEMIS missions and the empirical magnetic field model for the 17–19 March 2015 geomagnetic storm. (a–c) The X, Y, and Z components in GSM coordinates of the in situ external magnetic field measured by the Van Allen Probe A magnetometer (black line) compared with the storm datamining configuration (red line) of the model. (d) The X, Y, and Z components and radial distance in GSM coordinates of the Van Allen Probe A ephemeris in solid, dashed, dotted, and purple lines, respectively. (e–p) Matches (a–d) except for Van Allen Probes B, Cluster 2, and THEMIS A probe. (q) The OMNI solar wind measurements, showing the solar wind electric field parameter vB_z^{MF} (black line) and the dynamic pressure (orange line). (r) Geomagnetic indices $Sym-H^*$ (black line) and AL (orange line).

and the Radiation Belt Storm Probes Ion Composition Experiment (RBSPICE) instrument (Mitchell et al., 2013). The HOPE instrument uses an electrostatic analyzer and time-of-flight measurement to provide 3-D distributions of protons, helium, oxygen, and electrons from a few eV to ~55 keV. The time of flight by energy measurement from RBSPICE uses a time of flight and solid-state detector system to provide 3-D distributions of protons (~50–600 keV), helium (~65–870 keV), and oxygen (~130 keV to 1 MeV). To calculate the total pressure, the full HOPE energy range is used for all species along with RBSPICE protons above 60 keV and all energies of RBSPICE helium and oxygen. Long-term intercalibrations between the two instruments indicate that HOPE ion intensities need to be multiplied by a factor of 2 (for example, see discussion in Mouikis et al., 2019). Thus, they have been multiplied by two for this event. For each species and energy range, the perpendicular and parallel components of the pressure tensor are given by

$$P_{\perp} = 2\pi \sum_E \sum_{\alpha} \sqrt{2mE} J(E, \alpha) \frac{\sin^3 \alpha}{2} \Delta E \Delta \alpha \quad (13)$$

$$P_{\parallel} = 2\pi \sum_E \sum_{\alpha} \sqrt{2mE} J(E, \alpha) \sin \alpha \cos^2 \alpha \Delta E \Delta \alpha \quad (14)$$

where m is the ion mass, E is the middle energy of the energy channel, ΔE is width of the energy channel, α is the pitch angle, $\Delta \alpha$ is the pitch angle bin width, and J is the differential flux for a given energy and pitch angle.

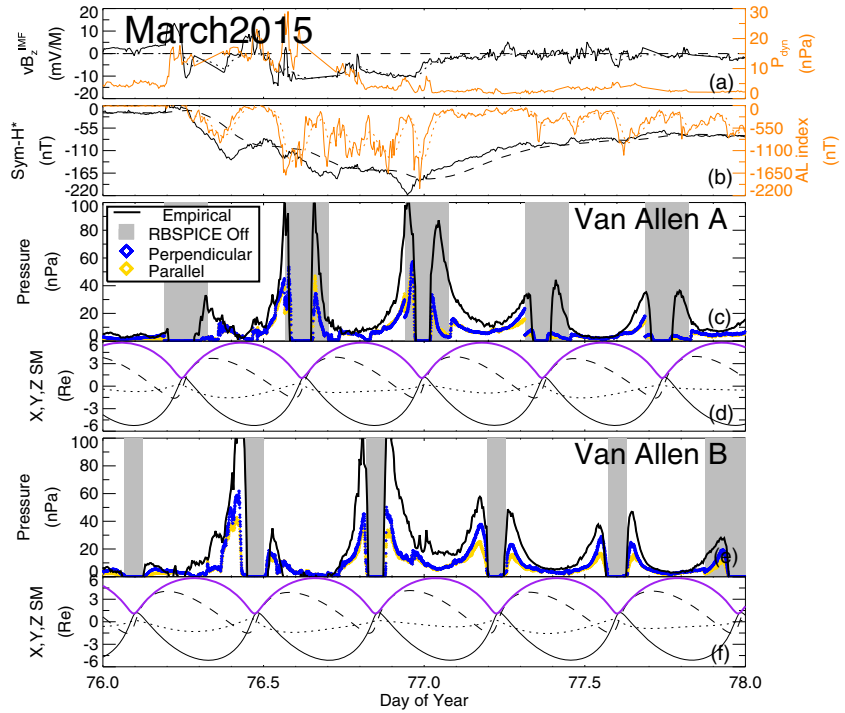


Figure 5. Comparison between the observed plasma pressure from the Van Allen Probes and the pressure reconstructed from the empirical magnetic field model for the 17–19 March 2015 geomagnetic storm. (a) Geomagnetic indices $Sym-H^*$ (black line) and AL (orange line). (b) The OMNI solar wind measurements, showing the solar wind electric field parameter vB_z^{IMF} (black line) and the dynamic pressure (orange line). (c and e) The total plasma pressure computed by summing contributions from HOPE and RBSPICE perpendicular pressures (blue symbols) and parallel pressures (yellow symbols) as compared to the reconstructed pressure computed by mapping the spacecraft location to the equivalent untitled model and computing the pressure by performing a line integral of the force balance equation. The gray shading indicates times when the RBSPICE instrument is turned off and thus does not contribute toward the pressures. (d and f) The X , Y , and Z components and radial distance in GSM coordinates of the Van Allen Probes ephemeris in solid, dashed, dotted, and purple lines, respectively.

The measured Van Allen Probes total plasma pressures are plotted in Figures 5c and 5e, with the perpendicular (blue symbols) and parallel (yellow symbols) pressures indicated separately (gray shading denotes periods when the RBSPICE instrument is turned off and thus does not contribute to the pressure). However, a complication arises when trying to compare the in situ pressures observed in GSM to the empirical pressures, because the above line-integration procedure acts on the untitled model and thus determines the pressure in untitled space: $P^{(u)}(\mathbf{r}^{(u)})$. One solution would be to formulate the pressure computation using the tilted model $P(\mathbf{r}_{GSM})$; however, the time-dependent warped nature of the fields due to the dipole tilt angle effects makes this complicated. Another simpler solution is to transform the tilted position vectors \mathbf{r}_{GSM} to the equivalent position vector in the untitled model $\mathbf{r}^{(u)}$. This is done by first tracing the spacecraft position to the magnetic equator using the tilted model $\mathbf{B}_{tot}(\mathbf{r}_{GSM})$, which utilizes the isotropic pressure assumption. Now, because this point resides in the equatorial current system, the equivalent point in the untitled equatorial current system can be found by traversing the chain of coordinate transformations that define $\mathbf{B}_{eq}(\mathbf{r}_{GSM})$, that is: $\mathbf{r}_{GSM} \xrightarrow{(1)} \mathbf{r}_0 \xrightarrow{(2)} \mathbf{r}_0^{(u)} \xrightarrow{(3)} \mathbf{r}^{(u)}$, where (1) is the spatial rescaling to the baseline dynamical pressure coordinates, (2) is the “bowl-shaped” deformation discussed in section 2.1 and detailed in Tsyganenko (2014), and (3) is the inverse of (1). The result is a position in untitled coordinates which lies on the equatorial plane ($Z^{(u)} = 0$) allowing for direct computation of the empirical pressure using the inward radially directed line integral method described below (section 3.3.2). Thus, this procedure yields a way to construct the tilted pressure field $P(\mathbf{r}_{GSM})$ from the untitled pressure field $P^{(u)}(\mathbf{r}^{(u)})$. The result is plotted in Figure 5c and 5e in black; furthermore, Figures 6f and 7f overplot the Van Allen probes orbit mapped to the equatorial plane using this technique.

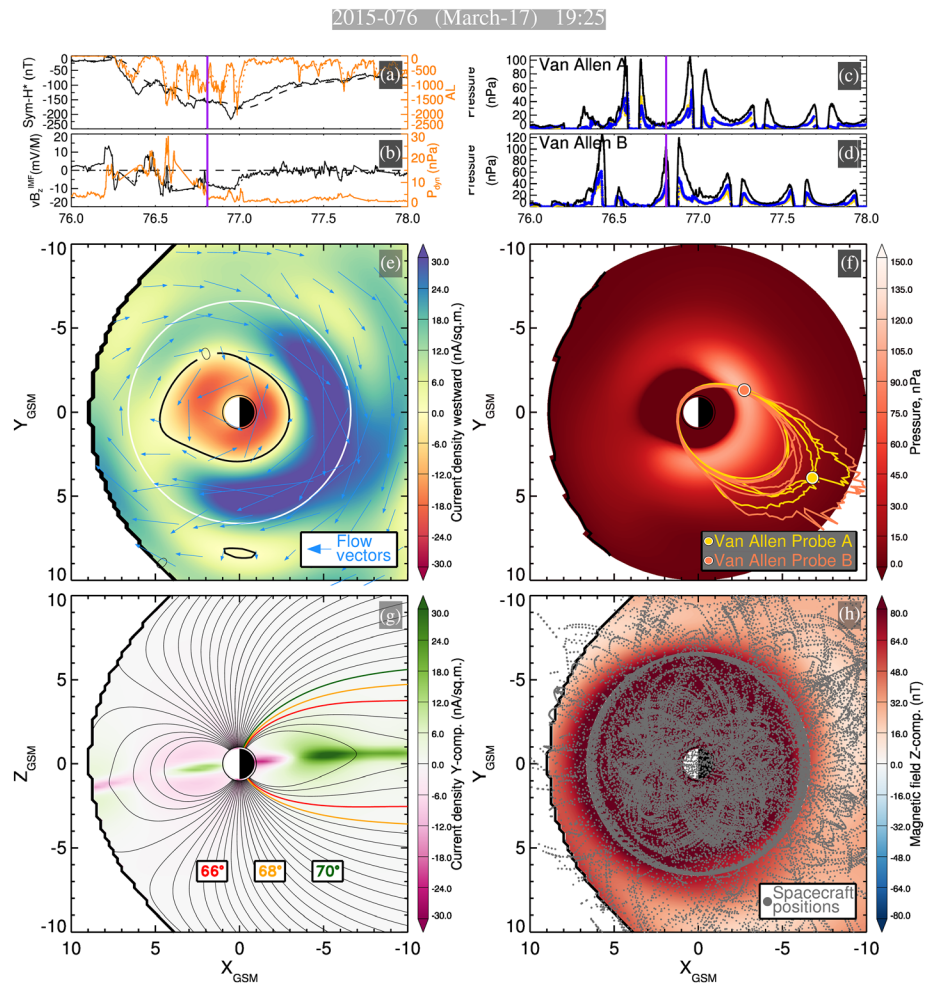


Figure 6. Reconstruction of the main phase of the 17–19 March 2015 storm. (a) Geomagnetic indices $Sym-H^*$ (black line) and AL (orange line). (b) The OMNI solar wind measurements, showing the solar wind electric field parameter vB_z^{IMF} (black line) and the dynamic pressure (orange line). (c and d) The reconstructed in situ pressure in a format similar to Figure 5 with a vertical purple line representing the moment in time. (e) The equatorial slice of the current density. The color represents westward component of the current density field, with green-blue representing westward and orange-red eastward flowing electric currents. The zero contour is overplotted in black. Flow vectors are overplotted in blue, indicating the direction and magnitude of the current flow. (f) The equatorial reconstruction of the pressure. The Van Allen Probe orbits mapped to the equatorial plane are overplotted in yellow and orange with the location at the moment of interest shown as circles. (g) The meridional slice of the Y component of the current density with magnetic field lines overplotted in black. (h) The equatorial slice of the total magnetic field. The equatorial projections of the spacecraft positions corresponding to the subset of magnetometer data used in fitting this moment in time are overplotted in gray.

Unfortunately, the RBSPIICE instrument was turned off (as indicated by the gray shading in Figure 5) during each pass through pressure peak on Van Allen Probe A, but the instrument was turned on Van Allen Probe B showing good qualitative consistency of the radial locations of the pressure peak during this storm. The major deviations are in the magnitude of the pressure peak. However, this is in the region where the isotropic pressure assumption is most invalid; note how the deviations between the parallel and perpendicular pressures are largest here. Given that perpendicular pressures are consistently greater than the parallel pressures, the pressure should be greater at the magnetic equator compared to the actual spacecraft location; thus, the empirical pressures are considered an upper limit to the anisotropic pressures observed by the spacecraft. The model also successfully reconstructs many of the large radial pressure gradients seen in the data, including the earthward boundary where the pressure effectively becomes 0. The pressures reach large values during this event, with the observed perpendicular pressures reaching as high as $P \gtrsim 50$ nPa

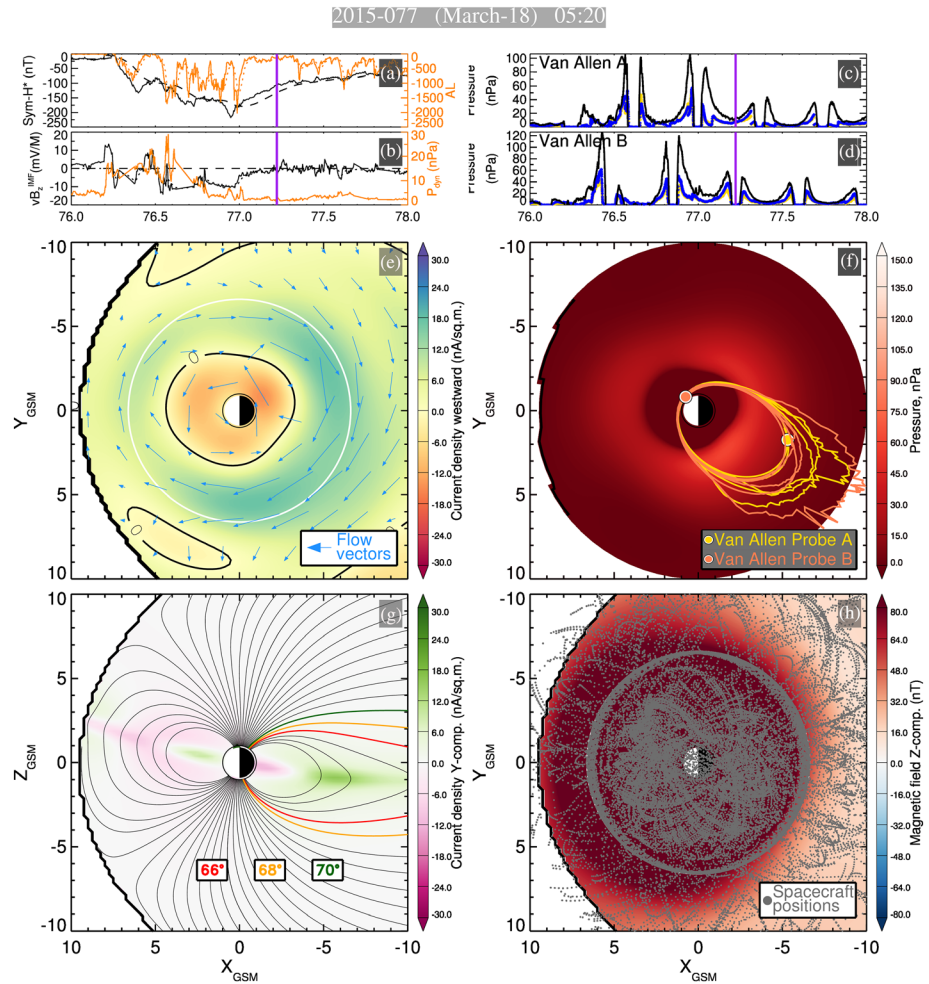


Figure 7. Reconstruction of the recovery phase of the 17–19 March 2015 storm. The panels are similar to Figure 6 except for a later moment in time.

and the empirical pressure topping $P > 100$ nPa during the main phase and remaining elevated above $P \approx 30$ nPa throughout the recovery phase.

3.2.2. March 2015 Global Distributions

The focus will now shift to the model's global reconstruction of the magnetic field, electric currents, and resulting pressure distributions for two different moments during the 17–19 March 2015 geomagnetic storm. These moments correspond to the later main and recovery phases, which are displayed in Figures 6 and 7 respectively. These figures show 2-D slices of the current density along the equatorial plane (panel e in Figures 6 and 7) and the meridional plane (panel g), along with the equatorial total B_z (panel h), and the resulting equatorial pressure distribution (panel f). The pressure is computed following the procedure described below (section 3.3.2) and is assigned a value of 0 beyond $r = 10 R_E$. The Van Allen Probes orbits have been mapped to the 2-D pressure distributions using the aforescribed mapping procedure. For simplicity and plotting convenience, all equatorial plots are created using a zero dipole tilt and twist parameter which aligns the magnetic equator with the equatorial plane. In contrast, the meridional panel demonstrates the effects of the tilt angle deformation.

The reconstruction of the main phase (17 March 2015, 19:25) of the storm is displayed in Figure 6 ($Sym-H^* = -161$ nT), showing the formation of a strong crescent like PRC spanning 12 hr in local time and centered about premidnight. The PRC is primarily located within geosynchronous orbit with a strong westward current density of $j > 30$ nA/m². This results in an azimuthally asymmetric pressure distribution that is stronger on the nightside with large pressures reaching $P \gtrsim 100$ nPa, which extends past the dusk terminator. Despite the

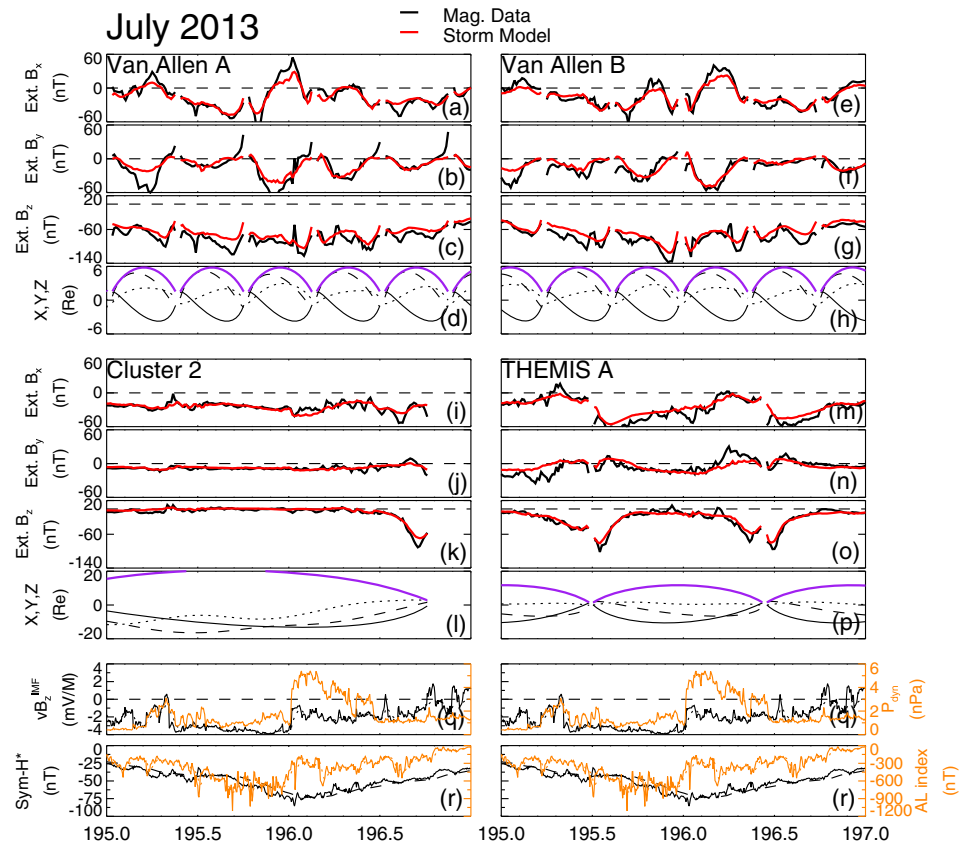


Figure 8. Comparison between the observed magnetic field from the Van Allen Probes, Cluster, and THEMIS missions and the empirical magnetic field model for the 13–15 July 2013 geomagnetic storm. The format is the same as Figure 4 except for a different event.

large degree of stretching indicated by Figure 6g, Van Allen Probe A is still within the integration region, meaning the spacecraft must be relatively close to the neutral plane (panels c and f), and the comparison of the pressures here (panel c) shows good agreement. Meanwhile, Van Allen Probe B is located very close to the pressure peak (panel d), which can be confirmed by the in situ particle pressures. It should also be noted that the current and pressure reconstruction is smoother and avoids artifacts from overfitting that were apparent in the earlier attempt at modeling the main phase of this event that did not include the distance-weighted KNN algorithm (Sitnov et al., 2018, their Figures 2 and 3).

The next time step (Figure 7) is about half a day later during the recovery phase of the storm (18 March 2015, 05:20). Due to the intensity of this storm, the activity level is still quite large with $Sym-H^* = -111$ nT. The ring current is now more symmetric but is still relatively strong with the nightside magnitude of the current density being $j \approx 15$ nA/m². Likewise, the pressure is also more symmetric but still strong with $P_{max} = 60$ nPa occurring at ~ 20 MLT while the dayside pressure is lesser but still relatively elevated at $P \approx 25$ nPa.

3.3. July 2013 Storm Reconstruction

The March 2015 storm was an intense and complex storm. In order to further analyze the pressure reconstruction and validation, the study now focuses on a simpler and more moderate storm. Between 13 and 15 July 2013, an interplanetary coronal mass ejection (ICME) swept over the Earth's magnetosphere generating a moderate intensity geomagnetic storm (Bingham et al., 2018). This storm followed immediately after two other moderate storms which occurred earlier in the month. The first full day (14 July 2013) was characterized by a relatively stable southward IMF with an electric field parameter of $vB_z^{IMF} \approx -4$ mV/M which acted to slowly decrease the value of $Sym-H^*$ to ~ -75 nT by the end of day. During this time AL was constantly active, indicating steady convection, permeated by substorm dipolarizations. The solar wind measurements and geomagnetic indices from the OMNI database are plotted in Figures 8q and 8r,

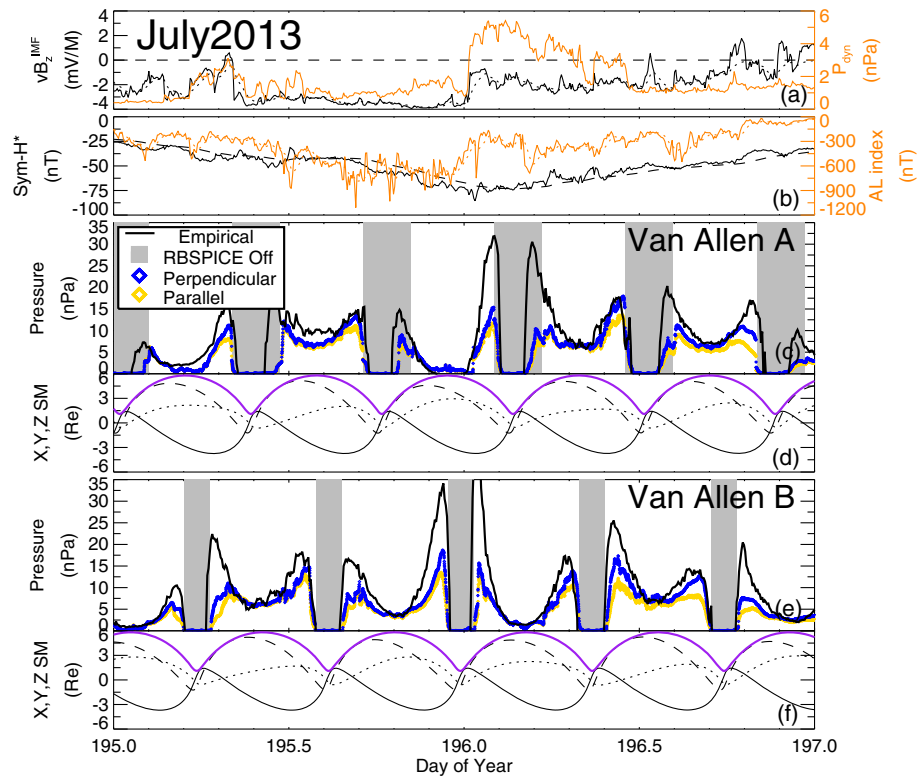


Figure 9. Comparison between the observed plasma pressure from the Van Allen Probes and the pressure reconstructed from the empirical magnetic field model for the 13–15 July 2013 geomagnetic storm. The format is the same as Figure 5 except for a different event.

respectively. The nature of the solar wind suddenly changed at the start of the next day (15 July 2013) as the solar wind dynamic pressure increased from ~ 1 to ~ 5 nPa within tens of minutes and remained elevated for about 11 hr. At this time, vB_z^{IMF} was about half of what it was the prior day, leading to a slow recovery in which AL was still active. Near the end of the day the IMF turned northward, ceasing AL activity. It should be noted that for moderate storms like this one, distance-weighting NNs is not necessary because there are numerous similar events in the database, regardless, the distance weighting is still applied for consistency.

During this time the Van Allen Probes' apogee was located at ~ 21 MLT and the two probes were nearly out of phase, resulting in complete orbit every ~ 4.5 hr. Three of the THEMIS probes were also oriented along the tail with apogees of $\sim 12 R_E$ and the four Cluster spacecraft were also in a tail configuration. The comparison between these spacecraft and the model is displayed in Figure 8. Overall, the reconstruction shows good consistency between the model and the six spacecraft observations. There are noticeable deviations (~ 40 nT) in B_y component of the magnetic field during the first 6 hr on 14 July 2013 as seen by both Van Allen Probes when they are at apogee; however, B_x and B_z are consistent. During this time the solar wind B_y^{IMF} is relatively negative, $B_y^{IMF} \approx -10$ nT; however, it remains steady throughout subsequent apogee passes when the measurements again match nicely with the observations. The only other major deviations occur near perigee, which routinely happens as it is difficult to isolate the components of the external magnetic field from the large approximately dipolar internal field.

The in situ comparison of the pressure in Figure 9 shows remarkable consistency between the model and observations at nearly every apogee pass. Fortunately, RBSPICE was turned on during each pass through pressure peak on both probes for this event. The radial location of the pressure peak also matches the majority of the time. Again, like the March 2015 storm, the major deviations are in the magnitude of the pressure peak, presumably caused by the particle pressure anisotropy here. The primary difference between the in situ pressure comparisons for this event and the March storm is the amplitude of the pressure

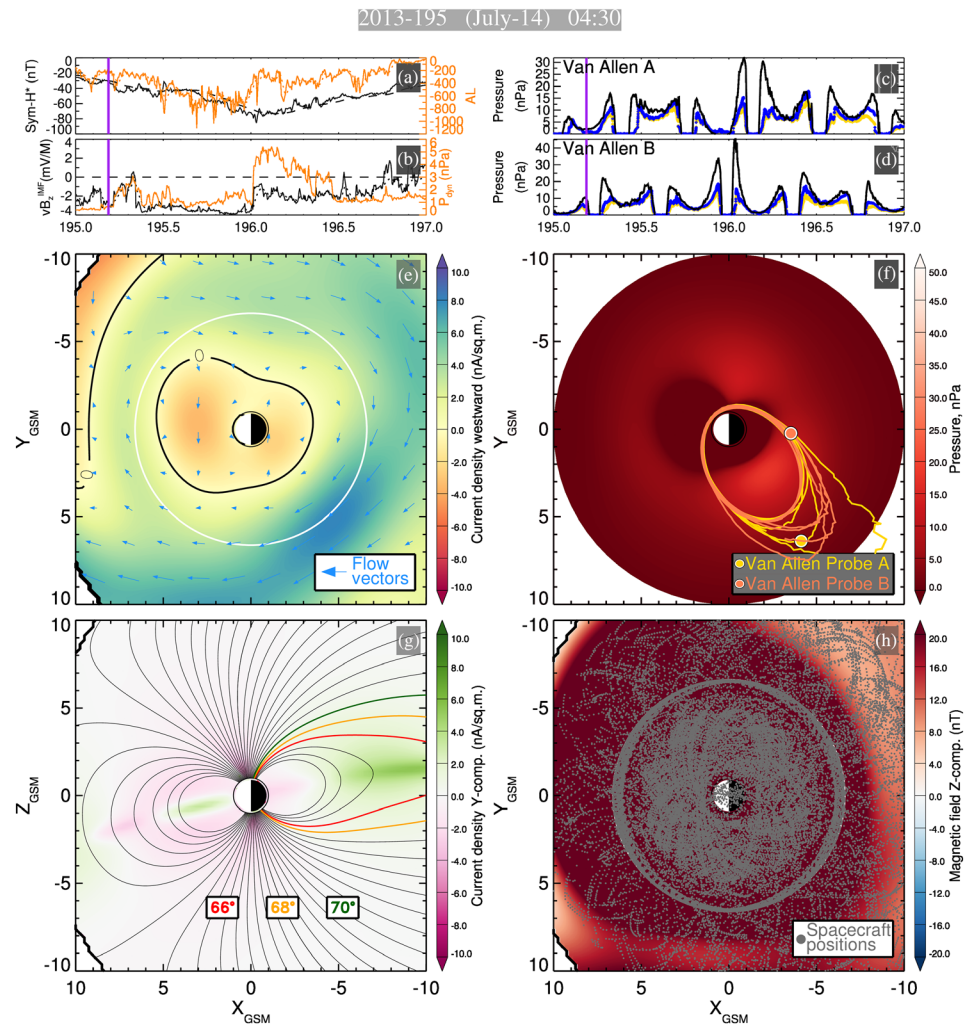


Figure 10. Reconstruction of the early main phase of the 13–15 July 2013 storm. The panels are similar to Figure 6 except for a different event.

enhancement throughout the main and recovery phases, with the observed perpendicular pressures only getting as high as $P \sim 18$ nPa and the empirical pressure topping $P > 35$ nPa during the main phase.

3.3.1. July 2013 Global Distributions

Again, the model's global reconstruction of the magnetic field, electric currents, and resulting pressure distributions are shown now for three different moments during the 13–15 July 2013 geomagnetic storm. These moments correspond to the early main, later main, and late recovery phases, which are displayed in Figures 10–12 respectively.

Figure 10 is from the early main phase of the storm (14 July 2013, 04:30), in which $Sym-H^* = -31$ nT. The solar wind dynamic pressure was particularly small ($P_{Dyn} < 0.5$ nPa) for the first several hours of this day, resulting in a large modeled magnetopause. The westward ring current shows a high degree of both dawn-dusk and night-day asymmetry, peaking about 21 MLT. Only a small amount of this current peak makes it to noon, with the majority appearing to outflow to the magnetopause. The resulting pressure distribution is also azimuthally asymmetric, with a peak value of $P_{max} = 17.9$ nPa located at $R_{Pmax} = 3.25 R_E$, 21 MLT, while the dayside pressure is weak having a pressure of $P \approx 5$ nPa. The nightside field lines are already stretching, causing the Van Allen Probes A position to map to a distance of $r = 7.6 R_E$; meanwhile, Van Allen Probes B is quite close to the pressure peak along midnight, which is confirmed by the data (Figure 10d). There appears to be a pressure peak near the planet at dawn, most likely because the model under evaluates the magnitude of the eastward current here.

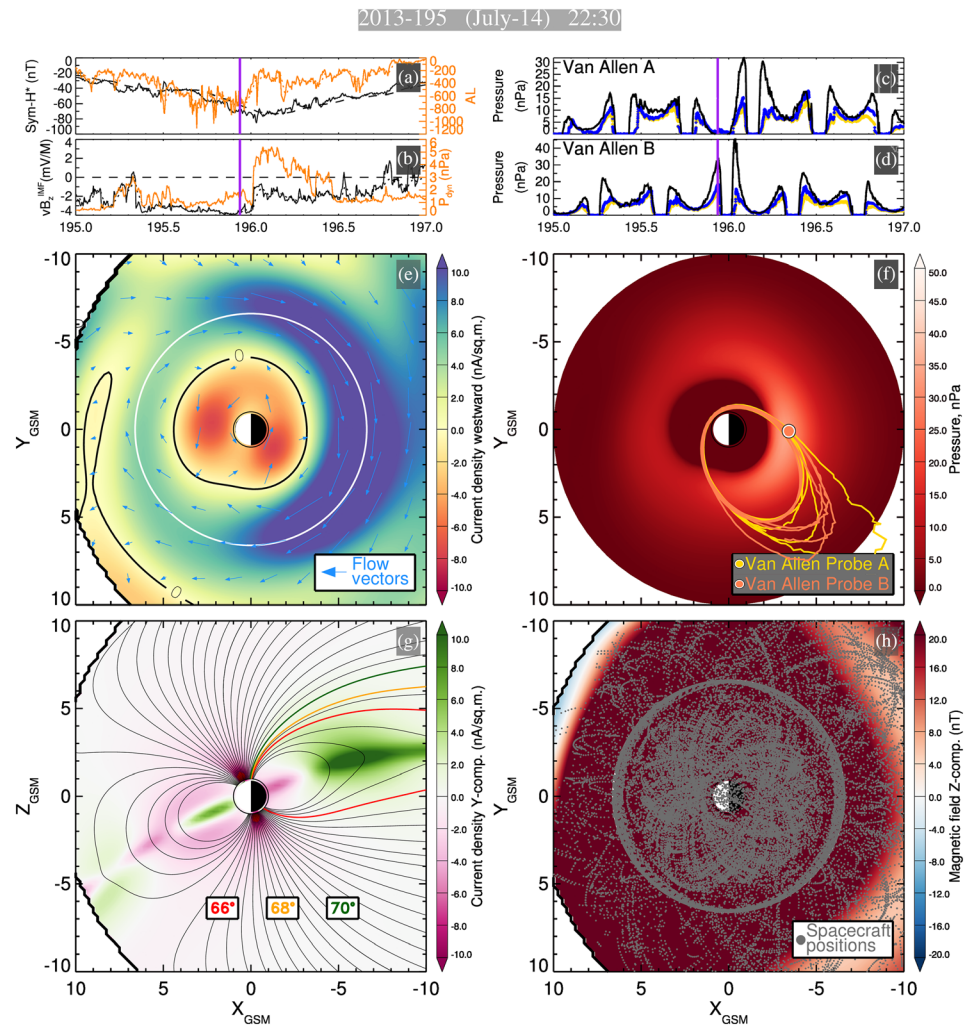


Figure 11. Reconstruction of the late main phase of the 13–15 July 2013 storm. The panels are similar to Figure 6 except for a different event.

The next step (Figure 11) is 18 hr later (14 July 2013, 22:30), during the main phase of the storm ($Sym-H^* = -65$ nT) when the decreasing rate of $Sym-H^*$ is near maximum, that is when $D(Sym-H^*)/Dt$ is near minimum. The solar wind is now a more typical value of $P_{Dyn} = 1.31$ nPa. The nightside ring current and pressure are much more dawn-dusk symmetric, although both are still stronger in the premidnight sector. The asymmetry in the westward ring current now primarily closes through the ionosphere generating a conventional PRC. The pressure is enhanced at all local times, but the peak has now shifted to close to midnight and has nearly doubled in its peak value $P_{max} = 34.2$ nPa but is still located at $R_{Pmax} = 3.25 R_E$. The nightside field lines are much more stretched, to the point that Van Allen Probe A now maps beyond the integration boundary and is assigned a zero pressure (Figure 11c). Van Allen Probe B is quite close to the pressure peak, which again has a similar location as compared to the data (Figure 11d). In comparison to the main phase reconstruction of the stronger March 2015 storm (Figure 6), the PRC is broader radially for this event and the magnitude of the current density is only about a third as intense. The stronger nightside pressure is more localized to the premidnight region than the March 2015 main phase where it instead encompasses about 12 hr in local time.

The last step (Figure 12) is nearly a day later in the late recovery phase (15 July 2013, 22:30). The storm index is actually quite similar to the first moment ($Sym-H^* = -34$ nT); however, the global configuration is entirely different. The westward and eastward ring currents along with the pressure are now highly azimuthally symmetric, resembling a conventional SRC with a peak current density near geosynchronous orbit. The pressure

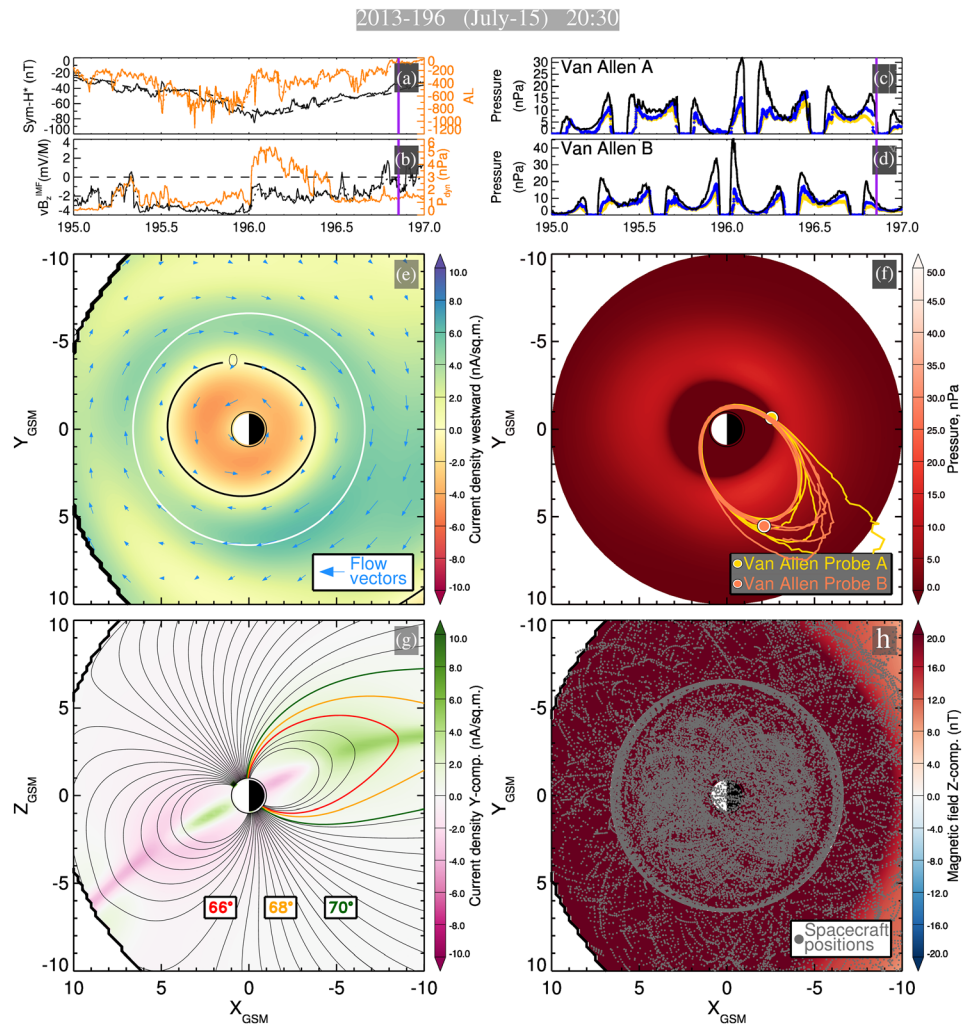


Figure 12. Reconstruction of the late recovery phase of the 13–15 July 2013 storm. The panels are similar to Figure 6 except for a different event.

peak is now $P_{max} = 16.1$ nPa and has migrated outward to $R_{Pmax} = 3.75 R_E$. The pressure is noticeable stronger on the dayside as compared to the early main phase, and the nightside field lines are now much more dipolar. The qualitative comparison between Figure 12, which is the late recovery phase, and the middle recovery phase of the March 2015 storm (Figure 7) shows how the PRC gradually fades becoming a conventional SRC during the course of the recovery phase.

3.3.2. Dependence of Plasma Pressure on Integration Path

If the magnetic field model is truly in isotropic force balance, then $\mathbf{j} \times \mathbf{B}$ would be a conservative vector field, and the resultant value of pressure from Equation 12 would be independent of the path. However, the model is in no way constrained to ensure the conservative property of $\mathbf{j} \times \mathbf{B}$, instead this is determined by the data.

In order to test the degree and regions in which $\mathbf{j} \times \mathbf{B}$ is and is not a conservative field, closed circular ($r_c = 0.25 R_E$) integrals are performed across the equatorial plane for the time slice 14 July 2013, 22:30 (discussed in detail above), corresponding to the late main phase of a geomagnetic storm, in which the ring current was highly asymmetric, thus representing a time when the quasi-static equilibrium assumption is most likely to be violated. The result displayed in Figure 13a reveals that $\mathbf{j} \times \mathbf{B}$ is nearly conservative except for the inner most region of the magnetosphere, in which it begins to be violated at $r \lesssim 3 R_E$ on the nightside and $r \lesssim 2 R_E$ on the dayside. This corresponds to the region where the magnitude of the internal magnetic field rapidly increases, meaning small errors in the knowledge of \mathbf{j} may

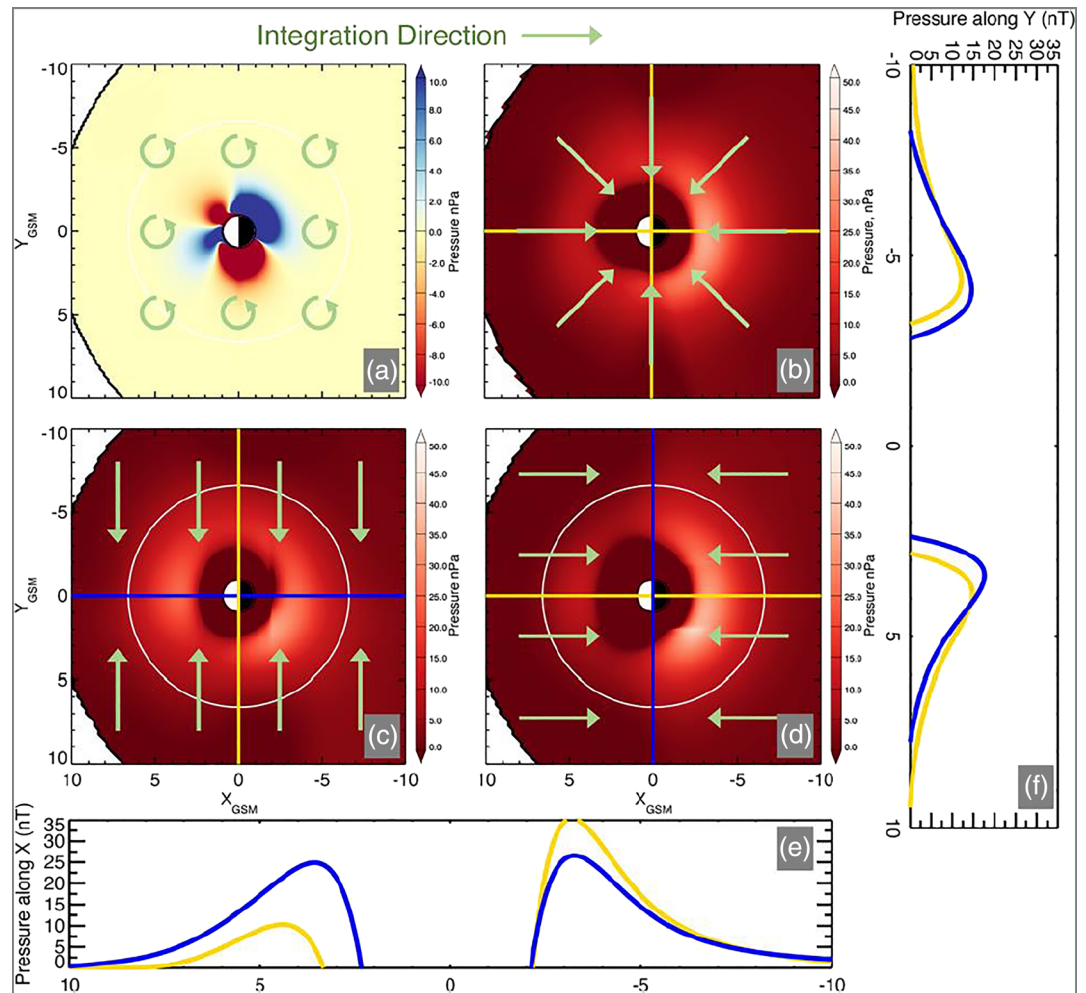


Figure 13. Pressure distributions computed from line integration of the $\mathbf{j} \times \mathbf{B}$ field and 1-D slices of those distributions along the X and Y axes. (a) The value of the pressure computed by integrating closed circles of radius $r_c = 0.25 R_E$. (b–d) The value of the pressure by integrating earthward from a boundary $r = 20 R_E$ or the magnetopause, whichever is closer, assuming that the pressure is 0 on that boundary, using different integration directions (shown by the green arrows). The integration directions are (b) radial, (c) along the Y axis, and (d) along the X axis. Panels (c) and (d) use the logistic function to sew together the dawn-dusk and day-night fields respectively. (e and f) One-dimensional slices of the pressure distributions along the X and Y axes, respectively, where the integration along the axis is shown in yellow and perpendicular to the axis is shown in blue.

cause $\mathbf{j} \times \mathbf{B}$ to be nonconservative. Furthermore, observations show that plasma anisotropy is greatest in this region as well (De Michelis et al., 1999; Lui & Hamilton, 1992; Tsyganenko, 2010).

Next, the 2-D pressure distributions are computed using three different integration paths. Ideally, if the integrations are performed from some pressure isosurface, then the resulting pressure distributions should be identical. However, this isosurface boundary is not known, so it is assumed that the pressure has a value of 0 at a circular radius of $r = 20 R_E$ or the magnetopause, whichever is closer. Figure 13d resembles the integration paths performed in earlier studies (Sergeev et al., 1994; Stephens et al., 2013) in which the nightside pressure is determined by integrating along +X, but with addition made by Sitnov et al. (2018), in which the dayside pressure is determined by integrating from the magnetopause along –X. The two solutions are sewn together in the vicinity of the Y axis using the logistic function. Figure 13c presents the same procedure except along the $\pm Y$ axis instead. The integration path used in Figure 13b is directed radially inward from the boundary. The line plots compare the 1-D profiles of the pressures along the X and Y axes. The X directed (panel d) and the inward radially directed (panel b) 2-D profiles are quite consistent, and the values of the pressure along the Y axis (blue for X directed and yellow for –r directed) are nearly indistinguishable

within geosynchronous orbit ($r \leq 6.6 R_E$). The Y directed pressure (panel c) is qualitatively consistent with the other two on the nightside, with a maximum in the pressure located $R_{Pmax} = 3.25 R_E$ at premidnight but is only about 70% as intense. The only major inconsistency is with the dayside pressure reconstruction, in which the Y directed integration is a factor of 2 larger, and the pressure peak is located about $1 R_E$ earthward in comparison to the other two. This appears to be caused an under resolved eastward ring current in the afternoon sector.

This justifies the use of the $-r$ directed integration path used throughout this study, as it appears to result in a similar configuration as the X directed and also minimizes the path through the region where $\mathbf{j} \times \mathbf{B}$ is non-conservative. The line plots indicate that the contribution to the pressure due to integrating beyond $r = 10 R_E$ is small, therefore justifying a circular radius of $r = 10 R_E$ or the magnetopause, whichever is closer, with a value of $P(\mathbf{r}_0) = 0$ as the boundary condition that was also used throughout the study.

4. Summary and Conclusion

In this study we have addressed a critical shortcoming of the KNN data mining approach to empirical magnetic field modeling caused by the inhomogeneity of points in the state space. When modeling dynamic times, such as storms and substorms, this inhomogeneity biases the model toward weaker events. This can be mitigated by including less magnetometer data points into the fit by decreasing the number of NNs K_{NN} ; however, this risks overfitting the model. An alternative solution is to simply give larger weights to NNs closer in the state space to the moment of interest, which are then propagated to the magnetometer records when the model is fit. This allows K_{NN} to be increased, reducing overfitting, while allowing data from stronger events to have a more significant impact on the magnetic field and current density reconstructions. This is particularly important in the reconstruction of extreme events as is discussed in our companion paper (Sitnov et al., 2020). Figure 3 shows the effectiveness of the distance-weighted KNN approach when using a simple Gaussian weighting function. The algorithm has room for further improvement. For example, Gaussian functions have very shallow tails, effectively eliminating NNs that fall in the tail of the distribution putting a constraint on how small a value of σ can be used, as observed in Figure 3c. Using a weighting function with heavier tails, such as the Student's t distribution, may help alleviate this problem. Furthermore, the Gaussian curve is symmetric, but because of the inhomogeneity of the NN state space, a Gaussian weighting cannot entirely eliminate the bias. This can potentially be addressed by using an asymmetrical distribution.

Next, we applied this distance-weighted KNN approach to model the 17–19 March 2015 “Saint Patrick’s Day” storm. The comparison between the observed and modeled magnetic field showed reasonable consistency as displayed in Figure 4, except that it did not always fully capture the magnitude of the large negative dips in B_z in the region between the westward and eastward current systems ($r \approx 4 R_E$). A plausible explanation is that although distance-weighting the NNs mitigates the bias toward weaker events, the bias is not eliminated. For example, Figure 2a demonstrates how the weighted mean of the NNs $G^{(WNN)}$ more closely tracks the storm intensity parameter $\langle Sym-H^* \rangle$ (the gap between the orange and black line is smaller than the gap between the purple and black line), but it still underestimates it particularly during the strongest part of the storm. Using a nonequal weighting of the storm state-space parameters (δ_j in Equation 3), in particular giving a larger weight to the $\langle Sym-H^* \rangle$ parameter, might help address this issue. Next, using the quasi-static equilibrium and isotropic pressure assumptions, the empirical pressure can be solved with the line integral $P(\mathbf{r}) - P(\mathbf{r}_0) = \int_C (\mathbf{j} \times \mathbf{B}) \cdot d\mathbf{r}'$, where \mathbf{j} is found from the model using Ampere’s law. As with previous studies (Sergeev et al., 1994; Sitnov et al., 2018; Stephens et al., 2013), the line integrals are simplified by ignoring dipole tilt angle effects, which aligns the magnetic equator and central plasma sheet with the equatorial plane.

We then performed a similar analysis on the moderate 13–15 July 2013 storm. The reconstructed picture was qualitatively similar to the March storm but with current and pressure magnitudes being approximately one third as large (Figures 10–12). Again, the empirical pressures largely matched the observed Van Allen Probes pressures including the radial location of the pressure peak R_{Pmax} (Figure 9).

This study demonstrates the importance of the eastward current in determining the empirical pressure. In the vicinity of the eastward current region ($r \lesssim 4 R_E$), the magnitude of background field is large and the magnitude of \mathbf{j} is small (relative to the westward current particularly during the main phase when the

PRC is large), meaning small errors in the knowledge of \mathbf{j} results in a drastically different $\mathbf{j} \times \mathbf{B}$. This is probably the cause of the nonconservative values of $\mathbf{j} \times \mathbf{B}$ close to the planet in the model as seen in Figure 13a. When integrating radially, the boundary between the eastward and westward ring currents define the location of the pressure peak. If the eastward current is not fully resolved, such as at dawn in Figure 10, R_{Pmax} is too small or is not resolved at all. Furthermore, if the eastward current is not sufficiently resolved across all local times, R_{Pmax} can become path dependent as was demonstrated in Figure 13c. While the additional thin current sheet used here certainly helps in resolving the eastward current, it is still not always sufficient, particularly when the ring current is weak. The resolution of this problem needs addressed in future studies.

Despite this issue, the comparison between the empirical pressure (by integrating along $-r$) and the observed pressure found by summing over Van Allen Probes energy and species is quite consistent as shown by Figures 5 and 9. The radial location of the pressure peak R_{Pmax} matches nearly every Van Allen Probes pass. The quantitative values of the pressures near the spacecraft's apogee are in great agreement. Closer to R_{Pmax} , the empirical pressures tend to overestimate the in situ pressures; this is expected due to the observed anisotropy in the pressure given that the empirical pressure is computed in the equatorial plane. Because the pressure was computed using a version of the model that ignored the dipole tilt effects, we developed a technique to map the position of the spacecraft to the equivalent position in the untilted field by traversing the coordinate transformation chain. The applications of this approach extends beyond just the pressure field to any other scalar quantities, such as the flux tube volume and plasma entropy, which are often computed on a flat 2-D plane (e.g., Stephens et al., 2013) for simplicity. Future studies should investigate the role of pressure anisotropy to see if it helps address the quantitative inconsistencies in the values of the pressure peak. One such method could use the knowledge of the particle pitch angle information to map the observed pressures to the magnetic equator. Another would be to reformulate the force balance Equation 11 without the isotropic assumption in a manner similar to the study performed by Tsyganenko (2010).

Another solution of the force balance equation is achieved by taking the divergence of each side of Equation 11 resulting in Poisson's equation (Zaharia & Cheng, 2003): $\nabla^2 P = \nabla \cdot (\mathbf{j} \times \mathbf{B})$. The pressure can be found using numerical methods for solving Poisson's equation with the appropriate boundary conditions again assuming a constant pressure along the field lines. It was argued by Zaharia and Cheng (2003) that the solution of this system is more consistent and removes the path integration uncertainty. However, the boundary conditions for the solution of Poisson's equation are quite complex (in particular, the external boundary includes a substantial part of the magnetopause and the cross tail segment) and uncertain (the inner boundary location and pressure values there). Thus, in the present study, the original approach of path integration of the force balance equation is used, which is complemented by the estimates of the uncertainty by comparing the results using different integration paths.

In conclusion, we have demonstrated that we can accurately reconstruct the time evolution of a 3-D isotropic plasma pressure, a key macroscopic parameter in plasma physics, in the inner magnetosphere during geomagnetic storms.

Acknowledgments

This work was funded by NASA grants NNX15AF53G, NNX16AB78G, NNX16AB80G, 80NSSC20K0601, and 80NSSC19K0074 and NSF grants AGS-1702147 and AGS-1744269. We thank the many spacecraft and instrument teams and their PIs who produced the data sets we used in this study, including the Cluster, Geotail, Polar, Imp-8, GOES, THEMIS, Van Allen Probes, and MMS, particularly their magnetometer teams. We also thank the SPDF for the OMNI database for solar wind values, which is composed of data sets from the IMP-8, ACE, WIND, Geotail, and DSCOVR missions and also the WDC in Kyoto for the geomagnetic indices.

Data Availability Statement

The compiled magnetometer database used in this study is available on the SPDF website (https://spdf.gsfc.nasa.gov/pub/data/aaa_special-purpose-datasets/empirical-magnetic-field-modeling-database-with-TS07D-coefficients/). The data used in the paper are archived on Zenodo (<https://doi.org/10.5281/zenodo.3942433>). This includes all the digital data that were used in constructing the figures from the text, along with files containing the fit set of coefficients and parameters for the model and files describing the subset of magnetometer used for fitting the model.

References

- Anderson, B. J., Korth, H., Waters, C. L., Green, D. L., Merkin, V. G., Barnes, R. J., & Dyrud, L. P. (2014). Development of large-scale Birkeland currents determined from the active magnetosphere and planetary electrodynamics response experiment. *Geophysical Research Letters*, *41*, 3017–3025. <https://doi.org/10.1002/2014GL059941>
- Anderson, B. J., Korth, H., Waters, C. L., Green, D. L., & Stauning, P. (2008). Statistical Birkeland current distributions from magnetic field observations by the Iridium constellation. *Annales Geophysicae*, *26*(3), 671–687. <https://doi.org/10.5194/angeo-26-671-2008>

- Auster, H. U., Glassmeier, K. H., Magnes, W., Aydogar, O., Baumjohann, W., Constantinescu, D., et al. (2008). The THEMIS fluxgate magnetometer. *Space Science Reviews*, *141*(1–4), 235–264. <https://doi.org/10.1007/s11214-008-9365-9>
- Baker, D. N., Jaynes, A. N., Kanekal, S. G., Foster, J. C., Erickson, P. J., Fennell, J. F., et al. (2016). Highly relativistic radiation belt electron acceleration, transport, and loss: Large solar storm events of March and June 2015. *Journal of Geophysical Research: Space Physics*, *121*, 6647–6660. <https://doi.org/10.1002/2016JA022502>
- Balogh, A., Dunlop, M. W., Cowley, S. W. H., Southwood, D. J., Thomlinson, J. G., Glassmeier, K. H., & Kivelson, M. G. (1997). The Cluster magnetic field investigation. *Space Science Reviews*, *79*(1/2), 65–91. <https://doi.org/10.1023/A:1004970907748>
- Bingham, S. T., Mouikis, C. G., Kistler, L. M., Boyd, A. J., Paulson, K., Farrugia, C. J., et al. (2018). The outer radiation belt response to the storm time development of seed electrons and chorus wave activity during CME and CIR storms. *Journal of Geophysical Research: Space Physics*, *123*, 10,139–10,157. <https://doi.org/10.1029/2018JA025963>
- Burton, R. K., McPherron, R. L., & Russell, C. T. (1975). An empirical relationship between interplanetary conditions and Dst. *Journal of Geophysical Research*, *80*(31), 4204–4214. <https://doi.org/10.1029/JA080i031p04204>
- Clausen, L. B. N., Baker, J. B. H., Ruohoniemi, J. M., Milan, S. E., & Anderson, B. J. (2012). Dynamics of the region 1 Birkeland current oval derived from the Active Magnetosphere and Planetary Electrodynamics Response Experiment (AMPERE). *Journal of Geophysical Research*, *117*, A06233. <https://doi.org/10.1029/2012JA017666>
- Cover, T. M., & Hart, P. E. (1967). Nearest neighbor pattern classification. *IEEE Transactions on Information Theory*, *13*(1), 21–27. <https://doi.org/10.1109/TIT.1967.1053964>
- De Michelis, P., Daglis, I. A., & Consolini, G. (1999). An average image of proton plasma pressure and of current systems in the equatorial plane derived from AMPTE/CCE-CHEM measurements. *Journal of Geophysical Research*, *104*(A12), 28,615–28,624. <https://doi.org/10.1029/1999JA900310>
- Funsten, H. O., Skoug, R. M., Guthrie, A. A., MacDonald, E. A., Baldonado, J. R., Harper, R. W., et al. (2013). Helium, Oxygen, Proton, and Electron (HOPE) Mass Spectrometer for the Radiation Belt Storm Probes mission. *Space Science Reviews*, *179*(1–4), 423–484. <https://doi.org/10.1007/s11214-013-9968-7>
- Gonzalez, W. D., Joselyn, J. A., Kamide, Y., Kroehl, H. W., Rostoker, G., Tsurutani, B. T., & Vasyliunas, V. M. (1994). What is a geomagnetic storm? *Journal of Geophysical Research*, *99*(A4), 5771. <https://doi.org/10.1029/93JA02867>
- Iyemori, T. (1990). Storm-time magnetospheric currents inferred from mid-latitude geomagnetic field variations. *Journal of Geomagnetism and Geoelectricity*, *42*(11), 1249–1265. <https://doi.org/10.5636/jgg.42.1249>
- Keika, K., Seki, K., Nosé, M., Miyoshi, Y., Lanzerotti, L. J., Mitchell, D. G., et al. (2018). Three-step buildup of the 17 March 2015 storm ring current: Implication for the cause of the unexpected storm intensification. *Journal of Geophysical Research: Space Physics*, *123*, 414–428. <https://doi.org/10.1002/2017JA024462>
- Kletzing, C. A., Kurth, W. S., Acuna, M., MacDowall, R. J., Torbert, R. B., Averkamp, T., et al. (2013). The Electric and Magnetic Field Instrument Suite and Integrated Science (EMFISIS) on RBSP. *Space Science Reviews*, *179*(1–4), 127–181. <https://doi.org/10.1007/s11214-013-9993-6>
- Liemohn, M. W., Ganushkina, N. Y., Katus, R. M., De Zeeuw, D. L., & Welling, D. T. (2013). The magnetospheric banana current. *Journal of Geophysical Research: Space Physics*, *118*, 1009–1021. <https://doi.org/10.1002/jgra.50153>
- Lui, A. T. Y., & Hamilton, D. C. (1992). Radial profiles of quiet time magnetospheric parameters. *Journal of Geophysical Research*, *97*(A12), 19,325–19,332. <https://doi.org/10.1029/92JA01539>
- Mauk, B. H., Fox, N. J., Kanekal, S. G., Kessel, R. L., Sibeck, D. G., & Ukhorskiy, A. (2013). Science objectives and rationale for the Radiation Belt Storm Probes mission. *Space Science Reviews*, *179*(1–4), 3–27. <https://doi.org/10.1007/s11214-012-9908-y>
- Mead, G. D., & Fairfield, D. H. (1975). A quantitative magnetospheric model derived from spacecraft magnetometer data. *Journal of Geophysical Research*, *80*(4), 523–534. <https://doi.org/10.1029/JA080i004p00523>
- Mitchell, D. G., Lanzerotti, L. J., Kim, C. K., Stokes, M., Ho, G., Cooper, S., et al. (2013). Radiation Belt Storm Probes Ion Composition Experiment (RBSPICE). *Space Science Reviews*, *179*(1–4), 263–308. <https://doi.org/10.1007/s11214-013-9965-x>
- Mitchell, T. M. (1997). *Machine learning* (first ed.). New York, NY: McGraw-Hill, Inc.
- Mouikis, C. G., Bingham, S. T., Kistler, L. M., Farrugia, C. J., Spence, H. E., Reeves, G. D., et al. (2019). The storm-time ring current response to ICMs and CIRs using Van Allen Probe observations. *Journal of Geophysical Research: Space Physics*, *124*, 9017–9039. <https://doi.org/10.1029/2019JA026695>
- Murphy, K. R., Mann, I. R., Rae, I. J., Waters, C. L., Frey, H. U., Kale, A., et al. (2013). The detailed spatial structure of field-aligned currents comprising the substorm current wedge. *Journal of Geophysical Research: Space Physics*, *118*, 7714–7727. <https://doi.org/10.1002/2013JA018979>
- Newell, P. T., Sotirelis, T., Liou, K., Meng, C.-I., & Rich, F. J. (2007). A nearly universal solar wind-magnetosphere coupling function inferred from 10 magnetospheric state variables. *Journal of Geophysical Research*, *112*, A01206. <https://doi.org/10.1029/2006JA012015>
- Perez, J. D., Goldstein, J., Mccomas, D. J., Valek, P., Fok, M.-C., & Hwang, K. J. (2016). Global images of trapped ring current ions during main phase of 17 March 2015 geomagnetic storm as observed by TWINS: Global images of ring current ions. *Journal of Geophysical Research: Space Physics*, *121*, 6509–6525. <https://doi.org/10.1002/2016JA022375>
- Press, W. H., Teukolsky, S. A., Vetterling, W. T., & Flannery, B. P. (1992). *Numerical recipes in Fortran 77* (2nd ed., pp. 51–63). Cambridge: Cambridge university press.
- Roelof, E. C. (1989). Remote sensing of the ring current using energetic neutral atoms. *Advances in Space Research*, *9*(12), 195–203. [https://doi.org/10.1016/0273-1177\(89\)90329-3](https://doi.org/10.1016/0273-1177(89)90329-3)
- Sergeev, V. A., Pulkkinen, T. I., Pellinen, T. I., & Tsyganenko, N. A. (1994). Hybrid state of the tail magnetic configuration during steady convection events. *Journal of Geophysical Research*, *99*(A12), 23,571–23,582. <https://doi.org/10.1029/94JA01980>
- Shue, J. H., Song, P., Russell, C. T., Steinberg, J. T., Chao, J. K., Zastenker, G., et al. (1998). Magnetopause location under extreme solar wind conditions. *Journal of Geophysical Research*, *103*(A8), 17,691–17,700. <https://doi.org/10.1029/98JA01103>
- Sitnov, M., Birn, J., Ferdousi, B., Gordeev, E., Khotyaintsev, Y., Merkin, V., et al. (2019). Explosive magnetotail activity. *Space Science Reviews*, *215*(4), 31. <https://doi.org/10.1007/s11214-019-0599-5>
- Sitnov, M. I., Stephens, G. K., Gkioulidou, M., Merkin, V. G., Ukhorskiy, A. Y., Korth, H., et al. (2018). Empirical modeling of extreme events: Storm-time geomagnetic field, electric current, and pressure distributions. In N. Buzulukova (Ed.), *Extreme events in geospace* (pp. 259–279). Amsterdam: Elsevier. ISBN: 9780128127001. <https://doi.org/10.1016/B978-0-12-812700-1.00011-X>
- Sitnov, M. I., Stephens, G. K., Tsyganenko, N. A., Miyashita, Y., Merkin, V. G., Motoba, T., et al. (2019). Signatures of nonideal plasma evolution during substorms obtained by mining multimission magnetometer data. *Journal of Geophysical Research: Space Physics*, *124*, 8427–8456. <https://doi.org/10.1029/2019JA027037>

- Sitnov, M. I., Stephens, G. K., Tsyganenko, N. A., Ukhorskiy, A. Y., Wing, S., Korth, H., & Anderson, B. J. (2017). Spatial structure and asymmetries of magnetospheric currents inferred from high-resolution empirical geomagnetic field models. In *Dawn-dusk asymmetries in planetary plasma environments* (pp. 199–212). Hoboken, NJ: John Wiley. <https://doi.org/10.1002/9781119216346.ch15>
- Sitnov, M. I., Stephens, G. K., Tsyganenko, N. A., Korth, H., Roelof, E. C., Brandt, P. C., et al. (2020). Reconstruction of extreme geomagnetic storms: Breaking the data paucity curse. *Space Weather*, *18*, e2020SW002561. <https://doi.org/10.1029/2020SW002561>
- Sitnov, M. I., Tsyganenko, N. A., Ukhorskiy, A. Y., Anderson, B. J., Korth, H., Lui, A. T. Y., & Brandt, P. C. (2010). Empirical modeling of a CIR-driven magnetic storm. *Journal of Geophysical Research*, *115*, A07231. <https://doi.org/10.1029/2009JA015169>
- Sitnov, M. I., Tsyganenko, N. A., Ukhorskiy, A. Y., & Brandt, P. C. (2008). Dynamical data-based modeling of the storm-time geomagnetic field with enhanced spatial resolution. *Journal of Geophysical Research*, *113*, A07218. <https://doi.org/10.1029/2007JA013003>
- Sitnov, M. I., Ukhorskiy, A. Y., & Stephens, G. K. (2012). Forecasting of global data-binning parameters for high-resolution empirical geomagnetic field models. *Space Weather*, *10*, S09001. <https://doi.org/10.1029/2012SW000783>
- Spence, H. E., Reeves, G. D., Baker, D. N., Blake, J. B., Bolton, M., Bourdarie, S., et al. (2013). Science goals and overview of the Radiation Belt Storm Probes (RBSP) Energetic Particle, Composition, and Thermal Plasma (ECT) Suite on NASA's Van Allen Probes mission. *Space Science Reviews*, *179*(1–4), 311–336. <https://doi.org/10.1007/s11214-013-0007-5>
- Stephens, G. K., Sitnov, M. I., Kissinger, J., Tsyganenko, N. A., McPherron, R. L., Korth, H., & Anderson, B. J. (2013). Empirical reconstruction of storm time steady magnetospheric convection events. *Journal of Geophysical Research: Space Physics*, *118*, 6434–6456. <https://doi.org/10.1002/jgra.50592>
- Stephens, G. K., Sitnov, M. I., Korth, H., Tsyganenko, N. A., Ohtani, S., Gkioulidou, M., & Ukhorskiy, A. Y. (2019). Global empirical picture of magnetospheric substorms inferred from multimission magnetometer data. *Journal of Geophysical Research: Space Physics*, *124*, 1085–1110. <https://doi.org/10.1029/2018JA025843>
- Stephens, G. K., Sitnov, M. I., Ukhorskiy, A. Y., Roelof, E. C., Tsyganenko, N. A., & Le, G. (2016). Empirical modeling of the storm time innermost magnetosphere using Van Allen Probes and THEMIS data: Eastward and banana currents. *Journal of Geophysical Research: Space Physics*, *121*, 157–170. <https://doi.org/10.1002/2015JA021700>
- Stern, D. P. (1987). Tail modeling in a stretched magnetosphere: 1. Methods and transformations. *Journal of Geophysical Research*, *92*(A5), 4437–4448. <https://doi.org/10.1029/JA092iA05p04437>
- Thébault, E., Finlay, C. C., Beggan, C. D., Alken, P., Aubert, J., Barrois, O., et al. (2015). International geomagnetic reference field: The 12th generation. *Earth, Planets and Space*, *67*(1), 79. <https://doi.org/10.1186/s40623-015-0228-9>
- Tsyganenko, N. A. (1989). A magnetospheric magnetic field model with a warped tail current sheet. *Planetary and Space Science*, *37*(1), 5–20. [https://doi.org/10.1016/0032-0633\(89\)90066-4](https://doi.org/10.1016/0032-0633(89)90066-4)
- Tsyganenko, N. A. (1991). Methods for quantitative modeling of the magnetic field from Birkeland currents. *Planetary and Space Science*, *39*(4), 641–654. [https://doi.org/10.1016/0032-0633\(91\)90058-1](https://doi.org/10.1016/0032-0633(91)90058-1)
- Tsyganenko, N. A. (1995). Modeling the Earth's magnetospheric magnetic field confined within a realistic magnetopause. *Journal of Geophysical Research*, *100*(A4), 5599–5612. <https://doi.org/10.1029/94JA03193>
- Tsyganenko, N. A. (1996). Effects of the solar wind conditions on the global magnetospheric configuration as deduced from data-based field models, in *Proceedings of the ICS-3 Conference on Substorms*, Eur. Space Agency Spec. Publ., ESA SP-389, 181.
- Tsyganenko, N. A. (1998). Modeling of twisted/warped magnetospheric configurations using the general deformation method. *Journal of Geophysical Research*, *103*(A10), 23,551–23,563. <https://doi.org/10.1029/98JA02292>
- Tsyganenko, N. A. (2002a). A model of the magnetosphere with a dawn-dusk asymmetry, 1. Mathematical structure. *Journal of Geophysical Research*, *107*(A8), 1179. <https://doi.org/10.1029/2001JA000219>
- Tsyganenko, N. A. (2002b). A model of the near magnetosphere with a dawn-dusk asymmetry, 2. Parameterization and fitting to observations. *Journal of Geophysical Research*, *107*(A8), 1176. <https://doi.org/10.1029/2001JA000220>
- Tsyganenko, N. A. (2010). On the reconstruction of magnetospheric plasma pressure distributions from empirical geomagnetic field models. *Journal of Geophysical Research*, *115*, A07211. <https://doi.org/10.1029/2009JA015012>
- Tsyganenko, N. A. (2013). Data-based modeling of the Earth's dynamic magnetosphere: A review. *Annales Geophysicae*, *31*(10), 1745–1772. <https://doi.org/10.5194/angeo-31-1745-2013>
- Tsyganenko, N. A. (2014). Data-based modeling of the geomagnetosphere with an IMF-dependent magnetopause. *Journal of Geophysical Research: Space Physics*, *119*, 335–354. <https://doi.org/10.1002/2013JA019346>
- Tsyganenko, N. A., & Sitnov, M. I. (2005). Modeling the dynamics of the inner magnetosphere during strong geomagnetic storms. *Journal of Geophysical Research*, *110*, A03208. <https://doi.org/10.1029/2004JA010798>
- Tsyganenko, N. A., & Sitnov, M. I. (2007). Magnetospheric configurations from a high-resolution data-based magnetic field model. *Journal of Geophysical Research*, *112*, A06225. <https://doi.org/10.1029/2007JA012260>
- Vassiliadis, D. (2006). Systems theory for geospace plasma dynamics. *Reviews of Geophysics*, *44*, RG2002. <https://doi.org/10.1029/2004RG000161>
- Vasyliunas, V. M. (1970). Mathematical models of magnetospheric convection and its coupling to the ionosphere. In B. M. McCormac (Ed.), *Particles and fields in the magnetosphere. Astrophysics and space science library, A series of books on the recent developments of space science and of general geophysics and astrophysics published in connection with the journal space science reviews* (Vol. 17, pp. 60–71). Dordrecht: Springer. https://doi.org/10.1007/978-94-010-3284-1_6
- Wolf, R. A. (1983). The quasi-static (slow-flow) region of the magnetosphere. In R. L. Carovillano & J. M. Forbes (Eds.), *Solar-terrestrial physics* (pp. 303–368). Dordrecht, Netherlands: Springer.
- Zaharia, S., & Cheng, C. Z. (2003). Can an isotropic plasma pressure distribution be in force balance with the T96 model field? *Journal of Geophysical Research*, *108*(A11), 1412. <https://doi.org/10.1029/2002JA009501>